REPUBLIQUE ALGERIENNE DEMOCRATIQUE ET POPULAIRE

MINISTERE DE L'ENSEIGNEMENT SUPERIEUR ET DE LA RECHERCHE SCIENTIFIQUE

Université 20 août 1955-Skikda

Faculté des Sciences

Département de Physique

Thèse de Doctorat LMD

Filière: Physique - Spécialité: Physique des Matériaux

Présentée par

M^me^ Fatima Zohra GADOUCHE

Thème :

Elaboration and characterization, of Ba-Sn-O system, by chemical method: Application in photovoltaic.

----------oOo----------

Elaboration et caractérisation, du système Ba-Sn-O, par méthode chimique : Application dans le photovoltaïque

Soutenue le : 10/03/2024 à 17h 00

Devant le Jury composé de:

Mr. Kamel KHOUNFAIS	Prof.	Université de Skikda	Président
Mr. Abdenour KABIR	Prof.	Université de Skikda	Rapporteur
Mr. Ali HAFS	MC-A	Université d'El Tarf	Examinateur
Mr. Abdelhak CHETTAH	Prof.	Université de Skikda	Examinateur

Année Universitaire : 2023/2024

Résumé:

L'effet de la substitution du baryum par le calcium et de l'étain par le plomb sur les propriétés structurales, optiques et luminescence des films de stannate de baryum déposés par spray pyrolyse sur des substrats en verre a été étudié dans ce travail, en fonction du rapport volumique de la solution à base de calcium R_{Ca} et le rapport volumique de la solution à base du plomb R_{Pb}. Les propriétés structurales, optiques et photoluminescence des films d'oxyde d'étain de baryum-calcium déposés ont été caractérisées par diffraction des rayons X (XRD), spectroscopie UV-visible et spectroscopie de photoluminescence (PL), respectivement. On a également mesuré l'épaisseur des films. Toutes les expériences ont été effectuées à une température du substrat de 500 °C.

La DRX a montré que la substitution du baryum par le calcium induit une transition de phase indirecte de Ba_3SnO à Ca_3SnO qui a été le même résultat pour la substitution de l'étain par le plomb durant la transition vers le Ba_3PbO. Des phases métastables ont été identifiées pour les deux séries d'échantillons. En fonction de R_{Ca}, la transmittance moyenne, dans le domaine visible, a augmenté de 50 à 80% tandis que l'énergie du gap a diminué de 3,14 à 3,09 eV. Les spectres PL ont révélés que la substitution du baryum par le calcium et de l'étain par le plomb augmente la concentration d'oxygène double ionisé (V_O^{++}). Le comportement semi-conducteur et la présence de défauts ont rendu les films déposés des matériaux prometteurs pour l'optoélectronique, la détection de gaz et les dispositifs de conversion photovoltaïques.

Mots clés :

Oxyde d'étain de baryum; Substitution; Transition de phase; Énergie du gap, lacunes d'oxygène.

Abstract:

The effect of the substitution of barium by calcium and tin by lead on structural, optical and luminescence properties of spray deposited barium tin oxide films onto glass substrates was studied in this work, as a function of the calcium-based solution volume ratio R_{Ca} and lead-based solution volume ratio R_{Pb}. The structural, optical and photoluminescence properties of deposited barium-calcium tin oxide films were characterized by x-ray diffraction (XRD), UV-visible spectroscopy and photoluminescence spectroscopy (PL), respectively. Measurement of the films thickness has been also done. All experiments were done at a substrate temperature of 500°C. According to x-ray diffraction (XRD) patterns, the substitution of barium by calcium induced an indirect phase transition from Ba_3SnO to Ca_3SnO which is the same result for the substitution of tin by lead during the transition to Ba_3PbO. Metastable phases were identified for both series of samples. As a function of R_{Ca}, the mean transmittance, in the visible domain, increased from 50 to 80% while the band gap energy decreased from 3.14 to 3.09 eV. PL spectra revealed that the substitution of barium by calcium and the substitution of tin by lead increased the concentration of double ionized oxygen vacancies (V_O^{++}). The semiconducting behavior and the presence of defects made the deposited films promising materials for optoelectronics, gas sensing and photovoltaic conversion devices.

Keywords:

Barium tin oxide; Substitution; Phase transition; Band gap energy; Oxygen vacancies.

Contents

General Introduction **i**

Chapter I. Barium tin oxide thin films

I.1. Thin films 1

I.1.1. Definition of thin films 1

I.1.2. Principle of deposit of thin films 3

I.1.3. Formation of thin films 4

I.1.4. Thin film growth mechanism 6

I.1.5. Thin film growth modes 7

I.1.6. Application of thin films 8

I.1.7. Criteria of selection of deposition methods 9

I.1.8. Thin film deposition techniques 9

I.1.8.1. Physical deposition methods 11

I.1.8.2.Chemical deposition methods 15

I.2. Barium tin oxide compounds (Ba-Sn-O system) 18

I.2.1. ABO_3 perovskite oxides 19

I.2.1.1. History of perovskite 19

I.2.1.2. Perovskite oxides structure 19

I.2.1.3. Deviation from ideality 20

I.2.1.4. Stoichiometric aspects of the perovskite structure 22

I.2.1.5. Defects in perovskite structure 22

I.2.1.6. Physical properties of perovskite oxides 23

I.2.1.7. $BaSnO_3$ perovskite oxides 23

I.2.2. A_3BO anti-perovskite oxides 30

I.2.2.1. Anti-perovskite oxides structure 31

I.2.2.2. Physical properties of anti-perovskite oxides 31

I.2.2.3. Ba_3SnO anti-perovskite oxides 32

Chapter II. Experimental procedures

II.1. Chemical spray pyrolysis technique 37

II.1.1. General principle of spray pyrolysis process 37

II.1.2. Influence of deposition parameters on thin film properties 40

II.1.3. Choice of spray pyrolysis technique 42

II.1.4. Spray pyrolysis system set-up 42

II.1.5. Preparation of barium-calcium tin oxide and barium lead-tin oxide thin films 43

II.2. Characterization techniques 44

II.2.1. X-ray diffraction (XRD) 44

II.2.2. UV-visible spectroscopy 48

II.2.3. Photoluminescence spectroscopy 50

II.2.4.Profilometer 52

Chapter III. Results and discussion

III.1. Effect of the substitution of barium by calcium 54

III.1.1. XRD characterization 54

III.1.2. UV-visible spectroscopy characterization 59

III.1.3. Photoluminescence spectroscopy characterization 62

III.2. Effect of the substitution of tin by lead 64

III.1.1. XRD characterization 64

III.1.3. Photoluminescence spectroscopy characterization 68

General Conclusion 70

Bibliography 72

List of figures

Chapter I

Figure I.1: Schematic of thin film deposited on a glass substrate. 2

Figure I.2: Diagram of the steps of the thin film manufacturing process. 4

Figure I.3: Diagram of the nucleation of thin layers. a) The arrival of atoms on a substrate, b) The morphology of the substrate. 5

Figure I.4: Diagram representing coalescence. 6

Figure I.5: The growth of thin layers. a) Step after coalescence, b) Growth. 6

Figure I.6: Growth modes of a thin film. 7

Figure 1.7: Classification of thin film deposition techniques. 10

Figure I.8: The operating principle of sputtering. 11

Figure I.9: Cathodic sputtering: accelerated Ar^+ ions extract atoms from the target. 12

Figure I.11: Schematic diagram of the Pulsed Laser Deposition (PLD) technique. 14

Figure I.12: Schematic diagram of thermal evaporation system. 15

Figure I.13: Schematic diagram of thermal evaporation system. 16

Figure I.14: Synthesis of various forms of materials by the sol-gel method. 17

Figure I.15: Schematic diagram of chemical bath deposition system. 18

Figure I.16: Lev Aleksevich von Perovski and the perovskite mineral species ($CaTiO_3$). 19

Figure I.17: (a) The perovskite unit cell showing the positions of the *A* site, *B* site, and oxygen. (b) An alternate presentation of the same crystal showing a three-dimensional network of corner shared BO6 octahedra. 20

Figure I.18: Schematic illustration of the BO6 octahedral tilting in perovskite oxides with (a) rhombohedral, and (b) orthorhombic crystal structures. The rotational patterns are also indicated. Figure adapted from. 21

Figure I.19: (a) The periodic table highlighting the elements that can be incorporated into the perovskite structure. Elements shaded in green can go into the *A* site, while those in red can go into the *B* site. (b) Diverse functionalities of perovskite oxides and their derived structures. 24

Figure I.20: $BaSnO_3$ perovskite structure. 25

Figure I.21: (a) Calculated band structure and (b) corresponding density of states (DOS) of BSO. Figure adapted from. 26

Figure I.22: Room-temperature electron mobility in single crystals and epitaxial thin films of doped $BaSnO_3$. 27

Figure 1.23: Application for solar cell (a) Solar panels. (b) Cross section of solar cell (c) J-V curves and PCEs at a maximum power point for the best performing BLSO and TiO_2 based perovskite solar cell. (d) Long term photostability test under AM 1.5G illumination with a metal-halide lamp, including UV radiation for BLSO and TiO_2-based perovskite solar cell. 30

Figure I.24: Crystal structure of anti-perovskite oxide. 31

Figure I.25: Cubic structure of Ba_3SnO anti-perovskite oxide. 33

Figure I.26: The band structure of Ba_3SnO determined by applying PBE-mBJ potential. 34

Figure I.27: The density of states (total and partial) computed by applying PBE-mBJ potential. 34

Chapter II

Figure II.1: Schematic representation of spray pyrolysis. 38

Figure II.2: Schematic representation of the Bragg's equation. 45

Figure II.3: Illustration showing definition of β from X-ray diffraction peak. 46

Figure II.4: Diffractometer used for characterization of the deposited thin films. 47

Figure II.5: Schematic representation of UV-visible spectrophotometer. 48

Figure II.6: Determination of the optical gap by extrapolation the linear part of the curve. 50

Figure II.7: Formation and recombination of an exciton in a semiconductor. 51

Figure II.8: Photoluminescence of a thin film of PEPI (excitation wavelength is 405 nm, from a laser diode). 52

Figure II.9: Schematic of a stylus profilometer. 53

Chapter III

Figure III.1: XRD patterns of barium-calcium tin oxide thin films. 54

Figure III.2: Variation of the lattice parameter a as a function of calcium-based solution volume ratio R_{Ca}. 56

Figure III.3: Variation of: **a)** the crystallites size and **b)** the corresponding peaks intensity as a function of calcium-based solution volume ratio R_{Ca}. 58

Figure III.4: Optical transmittance spectra of barium-calcium tin oxide films deposited with calcium-based solution volume ratio R_{Ca} from 0 to 0.5. 60

Figure III.5: Variation of the mean transmittance and the films thickness as a function of calcium-based solution volume ratio R_{Ca}. 60

Figure III.6: Plot of (Alpha E) ^{2} as a function of the energy E (Inset: Variation of the band gap energy as a function of calcium-based solution volume ratio R_{Ca}). 61

Figure III.7: PL spectra of barium calcium tin oxide films deposited with calcium-based solution volume ratio R_{Ca} from 0 to 0.5. 62

Figure III.8: Example of a deconvolution of a PL spectrum. 63

Figure III.9: Variation of oxygen vacancies corresponding emission peaks areas as a function of calcium-based solution volume ratio R_{Ca}. 64

Figure III.10: XRD patterns of barium lead-tin oxide films. 65

Figure III.11: Variation of the lattice parameter of Ba_3SnO and Ba_3PbO as a function of lead-based solution volume ratio R_{Pb}. 66

Figure III.12: Variation, as a function of the lead-based solution volume ratio, of: a) the crystallite size and b) the XRD peaks intensity. 67

Figure III.13: PL spectra of barium lead-tin oxide thin films. 68

Figure III.14: Variation of oxygen vacancies related peaks area as a function of $R_{Pb.}$ 70

General introduction

General Introduction

Transparent conducting oxides (TCOs), which combine high optical transparency in visible wavelengths with high electrical conductivity, have a wide range of applications in various fields such as solar energy, flat panel displays, and smart coatings [1, 2]. Many oxide materials, such as ZnO, SnO_2, and In_2O_3, have been widely investigated. However, these well-known material systems are still having some drawbacks such as the instability of oxygen content, fatigue, and degradation. Thus, there has been a challenge to find an appropriate alternative transparent material to have better properties.

Oxide materials with the perovskite structure, having a chemical formula ABO_3 are the subject of immense focus due to their exceptional optoelectronic capabilities in recent decades. Perovskites have historically been considered compounds with various intriguing properties that are highly dependent on the crystal structure composition . Photovoltaic devices and other optoelectronic technologies, such as lasers and light-emitting diodes, have exhibited excellent performance using perovskite materials. Perovskites have emerged as potential compounds for manufacturing solar cells during the last decade, potentially meeting our rising energy needs by significantly harvesting solar energy.

In particular, barium tin oxides with the chemical formula $BaSnO_3$ are important transparent materials due to interesting physical properties and perovskite structures [3, 4]. $BaSnO_3$ (BSO) is an ideally cubic perovskite-type oxide. It behaves as an n-type semiconductor, which has a wide band gap and exhibits a high transmittance of more than 85% in the visible region. $BaSnO_3$ has been used in various fields such as physical sensors, epitaxial structure, and future photovoltaic technology [5, 6]. Recent research shows that BSO doped with lanthanum (La) shows great advantages of thin film formation. It has been reported that La-doped $BaSnO_3$ (BLSO) has a high mobility of 320 $cm^2 V^{-1}s^{-1}$ for carrier concentration of 8×10^{19} cm^{-3} and a band gap of more than 4 eV, which is significantly larger than those from typical

transparent conductive oxides. Consequently, BSO is a promising candidate for transparent conductor applications.

Similar to perovskite oxides, the anti-perovskite oxides with the chemical formula A_3BO (A = Mg, Ca, Sr, Ba, Eu, Yb and B = Si, Ge, Sn, Pb), have been attracting attention as an alternative platform for prospecting unique physical properties, such as superconductivity, electrolytic, electrostriction, piezoelectric, thermoelectric properties, magnetic and optical properties. The anti-perovskite oxides can be appear as non-metals, semiconductors, metals as well as superconductors therefore they have interesting material [7]. This makes them capable of being used in different applications.

The interesting properties of anti-perovskite oxides are due to their bulk Dirac fermions. Following the theoretical prediction that some materials in the anti-perovskite oxide family have three-dimensional Dirac fermions [8], a number of experimental and theoretical efforts have been devoted to exploring the possible presence of bulk Dirac fermions in anti-perovskite oxides[9-12]. The anti-perovskites carbide and nitride have been extensively studied but the family of oxides such as Ca_3SnO [13], and Ba_3SnO [14, 15] have been less investigated.

In particular, Barium tin oxide Ba_3SnO has revealed direct (Γ-Γ) and small band gap nature, which demonstrate significant of this anti-perovskite oxide for optoelectronic device applications. Barium tin oxide thin films can be synthesized by various deposition techniques such as PVD (physical vapor deposition) and CVD (chemical vapor deposition). Whatever technique is used, the obtained films are extremely influenced by the deposition parameters.

The aim of this work is to study the effect of the substitution of barium by calcium on structural, optical properties of barium tin oxide thin films deposited using chemical spray pyrolysis technique. The present thesis is organized in three chapters in addition to a general introduction and a general conclusion.

In the first chapter, we present the bibliographic overview of thin films by giving their definition, application, principal of deposit, growth mechanism and also the deposition methods, in the first section. In the second section, we first give an overview of the properties of ABO_3 perovskite oxides focusing on $BaSnO_3$, by introducing their structural, optical and electrical properties as well as their applications. Then, we discuss A_3BO anti-perovskite oxides focusing on Ba_3SnO, by introducing their structural, optical and electrical properties as well as their applications.

In the second chapter, first we present the deposition system used for preparation of barium–calcium tin oxide thin films using chemical spray pyrolysis. Then, we describe the different characterization techniques used to study the effect of the substitution of barium by calcium on structural, optical and luminescence properties of deposited barium tin oxide films.

The third chapter is essentially devoted to the presentation and discussion of the results of the structural, optical, and photoluminescence characterizations of barium–calcium tin oxide thin films, as a function of the calcium-based solution volume ratio R_{Ca} and barium lead-tin oxide, as a function of lead-based solution volume ratio R_{Pb}. These characterizations were performed by different techniques such as x-ray diffraction (XRD), UV-visible spectrophotometry, photoluminescence (PL) spectroscopy in addition to thickness measurements by surface profilometry.

Chapter I

Barium tin oxide thin films

In the first section of this chapter, we will present the bibliographic overview of thin films by giving their definition, application, principal of deposit, growth mechanism and also the deposition methods. In the second section , we will first give an overview of the properties of ABO_3 perovskite oxides focusing on $BaSnO_3$, by introducing their structural, optical and electrical properties as well as their applications. Then, we will discuss A_3BO antiperovskite oxides focusing on Ba_3SnO, by introducing their structural, optical and electrical properties as well as their applications.

I.1. Thin films

I.1.1. Definition of a thin film

A thin film of a material can be define that is an element of this material so that its thickness is greatly reduced, which is expressed with nanometers (1 to 100 m^{-9}).The small distance between the two boundary surfaces gives a disturbance of the physical, chemical and mechanical properties (Figure I.1). The essential difference between the material it's in the bulk state and it's the thin state related to the fact that the role of the boundaries in the properties is usually neglected in the bulk state of materials, but in the thin state, on the contrary, the effects related to the boundaries are preponderant and very important [16]. It is quite obvious that the lower the thickness, the greater the bidimensionality effect. Conversely, when the thickness of a thin layer exceeds a certain threshold, the effect of thickness will become minimal and the material will return to the well-known properties of the solid state of material [17]. The second essential characteristic of a thin layer is that, whatever the procedure used for its manufacture, a thin layer is always integral with a substrate on which it

is built (even if it sometimes happens that one separates the thin film of said substrate). Consequently, it will be imperative to take into account this major fact in the design, namely that the substrate has a very strong influence on the structural properties of the layer deposited therein. Thus a thin layer of the same material, of the same thickness may have substantially different physical properties depending on whether it will be deposited on an amorphous insulating substrate such as glass, or a monocrystalline silicon substrate, for example. The purpose of the thin layer is to give particular properties to the surface of the part while benefiting from the massive properties of the substrate (in general: mechanical resistance), for example:

* Electrical conductivity: metallization of the surface, for example to observe an insulating sample under a scanning electron microscope.

* Optical: mirror glass, anti-reflective treatment of camera lenses, nickel plating of fire elmets to reflect heat (infrared), gilding of their visor to avoid glare [18].

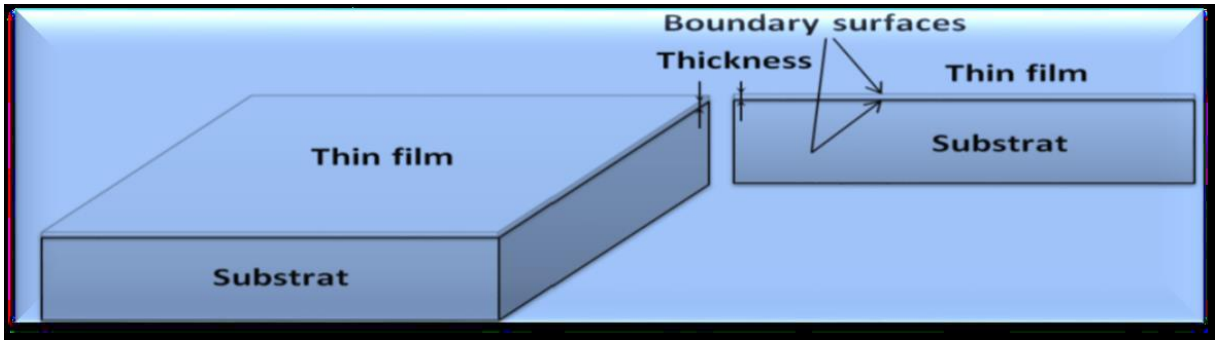

Figure I.1: Schematic of thin film deposited on a glass substrate [17].

I.1.2. Principle of deposit of thin films

To form a thin layer on a solid surface (substrate) the particles of the coating material must pass through a conductive medium until intimate contact with the substrate. When the

substrate arrives, a fraction of the coating particle adheres or reacts chemically with the substrate. The particles can be atoms, molecules, ions or fragments of ionized molecules. The transport medium can be solid, liquid, gas, or vacuum:

a) Solid: in this situation, the substrate is in contact with the solid, only the particles which diffuse from the solid towards the substrate form a layer. Often, it is very difficult to obtain thin films by contact between solids, for example: the diffusion of Oxygen from Silica to form a thin SiO_2 layer on a Silicon substrate.

b) Liquid medium: it is easier to use than the first case, because the material is more versatile in this state (epitaxy in liquid phase, and electrochemical, sol gel…).

c) Gas or vacuum: this is a CVD type deposit where the difference between the gaseous medium and the vacuum is the average free path of the particles. There is no standard thin film deposition method that can be used in different situations. Substrate preparation is often a very important step for thin layer deposits in order to obtain good adhesion [19].

I.1.3. Formation of thin films

The process of depositing a thin layer is carried out in three stages [20]:

- Synthesis or creation of the species to be deposited.
- Transport of these species from the source to the substrate.
- Deposition on the substrate and growth of the layer.

Depending on the process followed, these steps can be completely separate from each other or else superimposed. Figure I.2 illustrates, in general, the process steps involved in the development of thin layers [21].

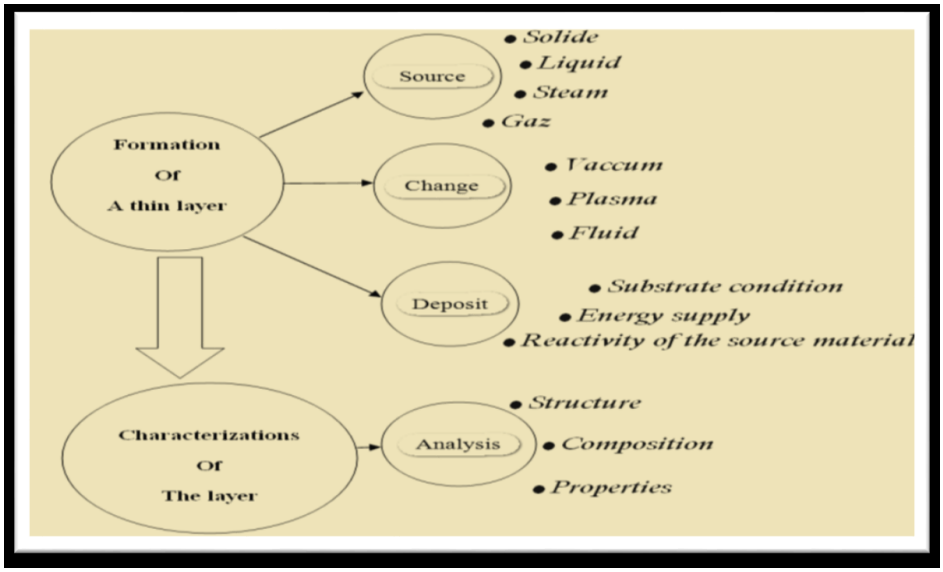

Figure I.2: Diagram of the steps of the thin film manufacturing process [21].

I.1.4. Thin film growth mechanism

All thin film processes are done in three stages:

- The production of appropriate ionic, molecular, atomic species.
- The transport of these species to the substrate.
- Condensation on this same substrate is done either directly or through a chemical or electrochemical reaction in order to form the solid deposit; this step often goes through three phases: nucleation, coalescence then growth.

a) Nucleation

It is the phenomenon that accompanies changes in the state of matter and which consists in the appearance, within a given medium, of transformation points from which a new physical or chemical structure develops.

The entire surface of it, in this state, they interact with each other and form what are called "clusters". These "clusters" also called nuclei, are unstable and tend to subside. Under certain

deposit conditions, they collide with other adsorbed species and start to grow. After reaching a critical size, these clusters become thermodynamically stable and the nucleation barrier is crossed. The nucleation stage is shown in figure I.3.

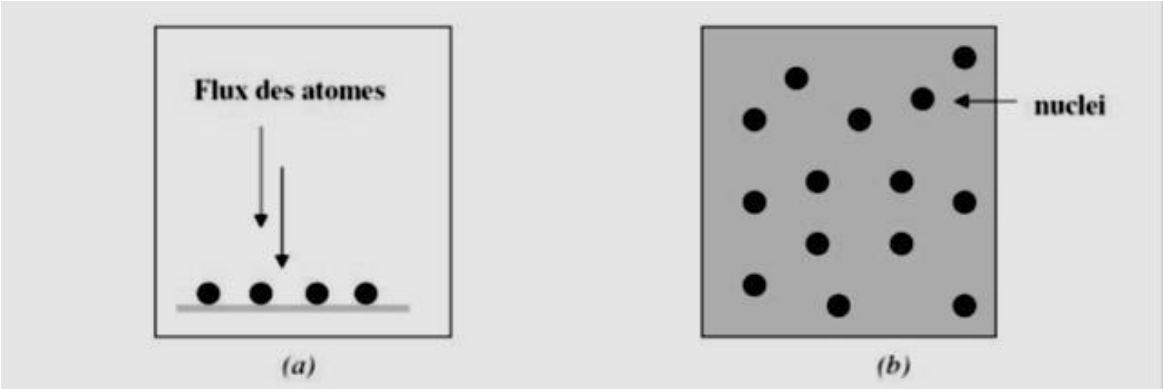

Figure I.3: Diagram of the nucleation of thin layers. a) The arrival of atoms on a substrate, b) The morphology of the substrate [22].

b) Coalescence

The nuclei grow in size but also in number until they reach a maximum nucleation density. This as well as the average size of these nucleus also called islets depend on a certain number of parameters such as the energy of the sprayed species, the rate of spraying, the energy of activation, adsorption, desorption, thermal diffusion, substrate temperature, topography and chemical nature of the substrates .

A nucleus can grow at the same time parallel to the substrate by a surface diffusion phenomenon of the pulverized species. It can also grow perpendicular to the substrate by adding sprayed species. In general the lateral growth in this stage is much more important than the perpendicular growth. Figure I.4 represents the phase of coalescence.

c) Growth

The last step in the film manufacturing process is the coalescing step in which the islets begin to cluster.

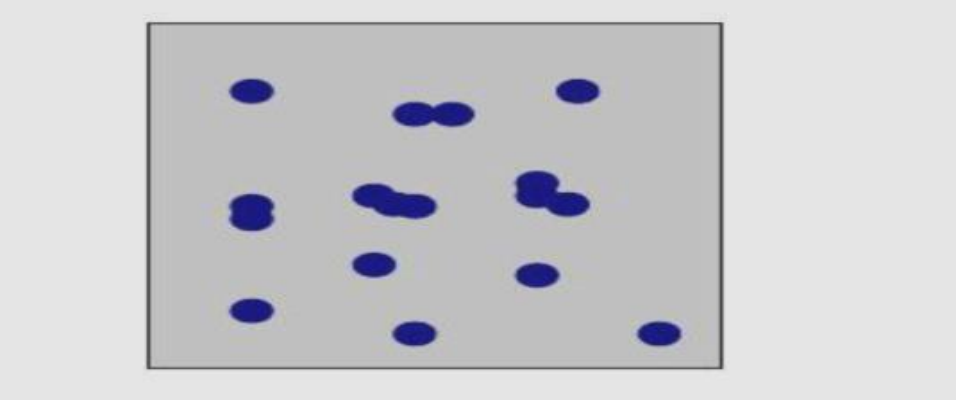

Figure I.4: Diagram representing coalescence [22].

This tendency to form larger islets is improved by the growth of the surface mobility of the adsorbed species. This improvement is obtained by increasing the temperature of the substrate. These larger islets still grow, leaving channels and holes on the substrate. The structure of the film in this step changes from a type of discontinuous islands to a type of porous networks. A continuous film is formed by filling the channels and the holes (Figure I.5) [22].

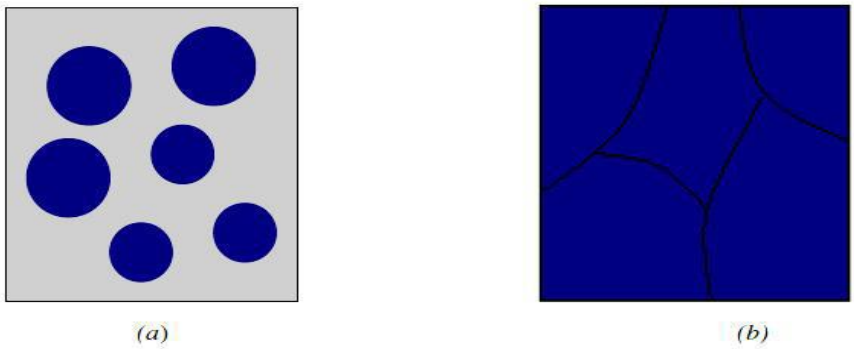

Figure I.5: The growth of thin layers. a) Step after coalescence, b) Growth [22].

I.1.5. Thin film growth modes

There are three modes of growth [23]:

a. 2D growth (known as Frank Van Der Merve)

On one side of a crystal, the atomic layers grow one after the other and the atomic surface remains flat during deposition (Figure I.6). This type of growth is expected when the bonding energy between the deposited atoms is less than or equal to that between the thin layer and the substrate.

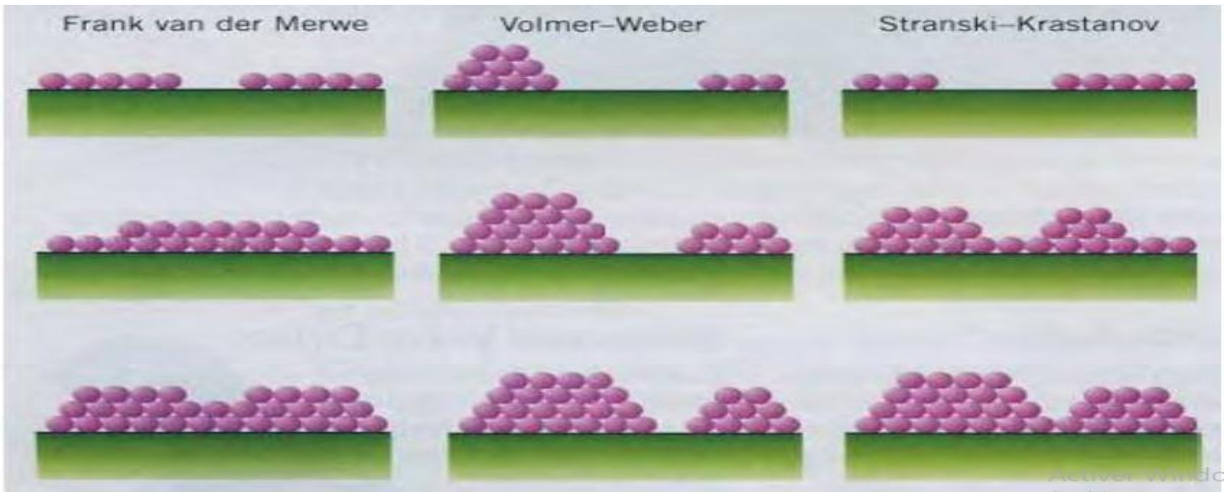

Figure I.6: Growth modes of a thin film [23].

b. 3D growth (known as Volmer-Weber)

In this mode of growth, islands are formed and it is their coalescence that will form a film (Figure I.6). This mode of growth will take place when the atoms forming the deposited layer are more strongly bound together than with the substrate.

c. Mixed growth (Stranski-Krastanov)

It is a growth that begins like that of Frank Van-der-Merve (Growth 2D) but after a few atomic layers the growth becomes 3D (Figure I.6). We can model the transition of growth regime from the curve giving the energy of the deposited layer according to the number of layers. If it has an inflection point, the system will be unstable to fluctuations in heights beyond this inflection point, which will tend towards the formation of 3D islands when the critical thickness is exceeded.

I.1.6. Applications of thin films

During 20th century, more sophisticated applications diversified in the following fields [24, 25].

Microelectronics: It was developed from the 1960s thanks to the use of increasingly thin conductive or insulating layers, and can be found under types of passivating layers (electronic contact), PN junction, transistor diode, piezoelectricity, laser, LED lamps, superconductors, etc.

Optics: While retaining the aesthetic applications, the optical applications of the layers have made it possible to develop more effective radiation sensors, such as antireflective layers in solar cells, anti-reflective treatment of camera lenses, photo detection, display of screens dishes, ophthalmic applications, optical guides (architecture energy checks, vehicles, energy conversion, etc.).

Mechanics: Tribological coatings (dry lubrication, resistance to wear, erosion, abrasion, diffusion barriers) micro-systems…etc.

Chemistry: The main applications of surface coatings are oriented towards better corrosion resistance by the creation of a waterproof film (corrosion resistance), gas sensor, catalytic coatings and protective layers.

Thermal: The use of a thermal barrier layer (TBC) decreases for example the surface temperature of the metal of the fins of the reactors thus making it possible to improve the performances of the reactors (increase in the internal temperature).

Biology: Biological micro sensors, biochips, biocompatible materials…etc.

Micro and Nanotechnologies: Mechanical and chemical sensors, micro fluidics, actuators, detectors, adaptive optics, nano-photonics…etc.

Magnetic: Information storage (computer memory), security devices, sensors.

Decoration: Watches, glasses, jewelry, household equipment, etc [26].

I.1.7. Criteria for selection of deposition methods

The selection of a specific technology for the deposition of thin films can be based on a variety of considerations. A multitude of thin films of different materials can be deposited for a large variety of applications; hence, no general guidelines can be given of what the most suitable deposition technology should be. In selecting an appropriate deposition technology for a specific application, several criteria have to be considered. In order to optimize the desired film characteristics, a good comprehension of the advantages and restrictions applicable to each technique is necessary. The choice of a specific deposition technique related to some factors, they are [18]:

- The material to be deposited.
- The rate of deposition.
- Limitations imposed by the substrate, e.g: maximum deposition temperature.
- Adhesion of the deposits to a substrate.
- Throwing power.
- The purity of target material.
- Availability of the required equipment.
- Cost.
- Ecological considerations.
- The abundance of the material (to be deposited).

I.1.8.Thin film deposition techniques

The methods employed for thin-film deposition can be divided into two groups based on the nature of the deposition process viz., physical or chemical. The physical methods include

physical vapor deposition (PVD), laser ablation, molecular beam epitaxy, and sputtering. The chemical methods comprise gas-phase deposition methods and solution techniques. The gas-phase methods are chemical vapor deposition (CVD) [27, 28] and atomic layer epitaxy (ALE) [29], while spray pyrolysis [30], sol-gel [31], spin- [32] and dip-coating [33] methods employ precursor solutions. The different physical and chemical methods of thin films deposition are shown in figure I.7.

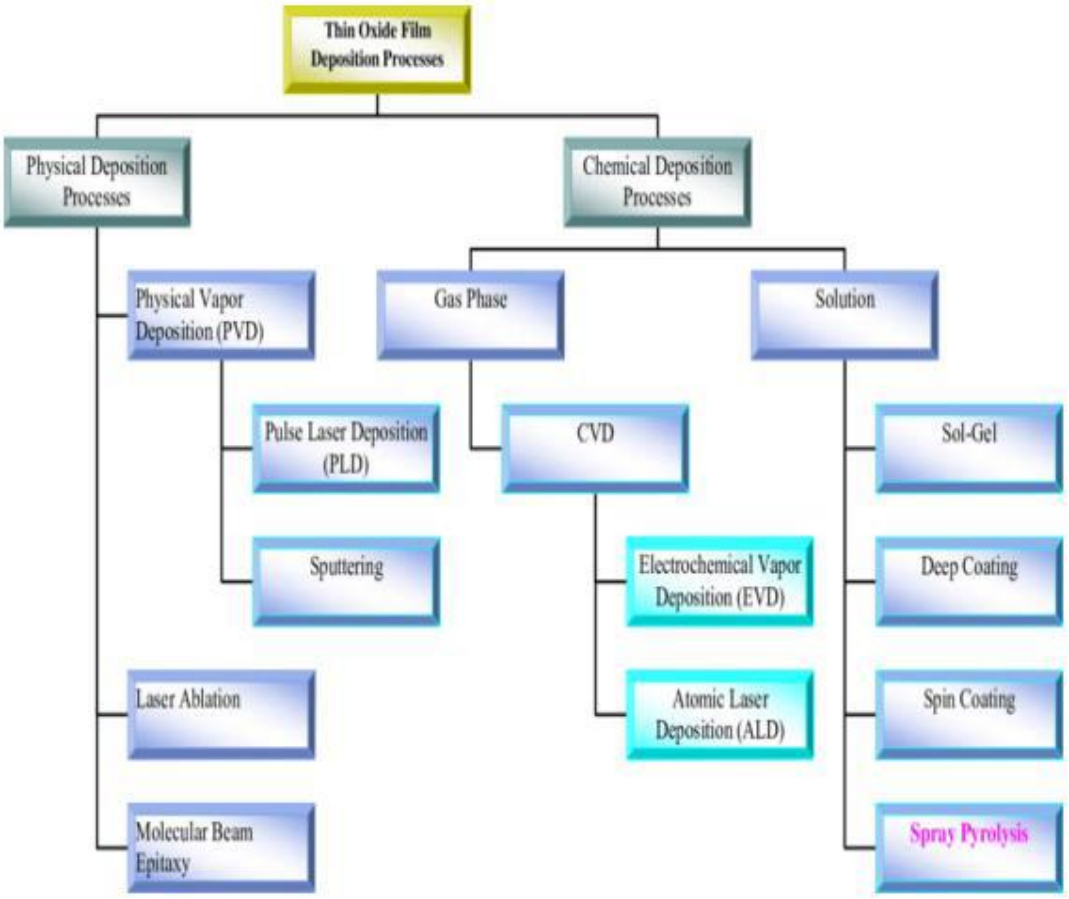

Figure 1.7: Classification of thin film deposition techniques.

I.1.8.1. Physical deposition methods

a. Sputtering

Sputtering is a technique used to deposit different materials such as metals, refractory materials, dielectrics, and ceramics. The principle of this technique is the bombardment of the material to be deposited (target) by neutral gas ions generally argon, under the effect of bombardment atoms torn from the target and deposits on the substrate located in front of the target. If the atmosphere (gas) of the discharge is chemically neutral, the sputtering is called simple. However, if it consists of active gases such as oxygen O_2 or nitrogen N_2, sputtering is said to be reactive. The basic scheme of operation of the sputtering is shown in figure I.8.

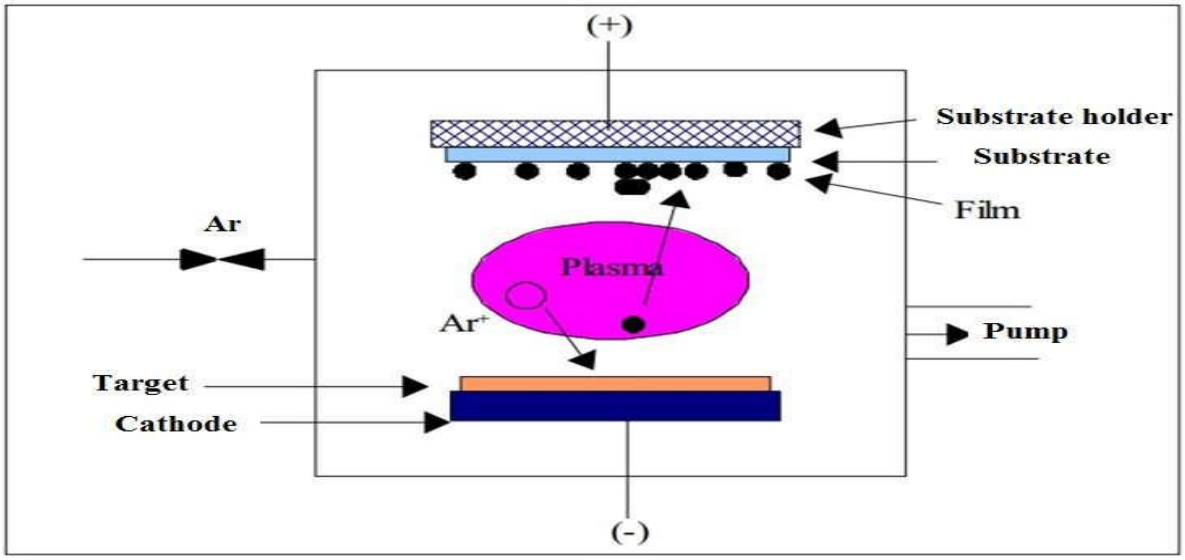

Figure I.8: The operating principle of sputtering [34].

There are two types of cathodic sputtering (Figure I.9) depending on the mode of creation of the plasma or the nature of the target (conductive or insulating): direct cathodic sputtering (DC) only in the case of the sputtering of conductive materials and sputtering radiofrequency (RF) which allows the spraying of conductive materials or insulating materials. There are many parameters that affect the deposition process such as base vacuum, sputter gas pressure

during deposition, sputter power, target and substrate temperature, etc…The magnetron device has been used to limit the disadvantages and increase the efficiency of the sputtering.

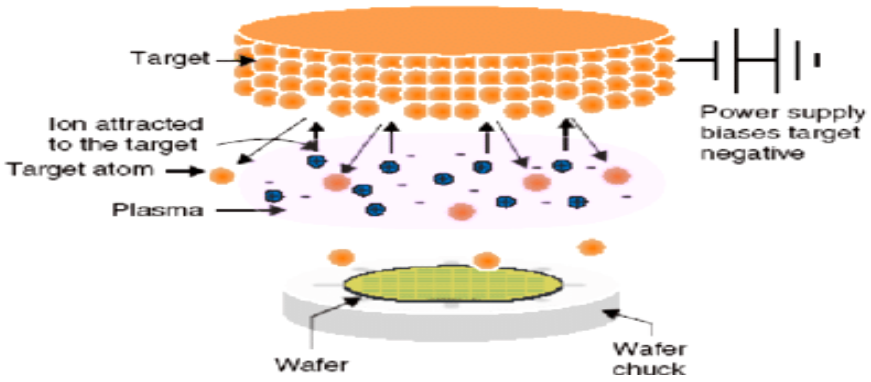

Figure I.9: Cathodic sputtering: accelerated Ar^+ ions extract atoms from the target [35].

b. Molecular Beam Epitaxy (MBE)

Epitaxy is a compound of two Greek words Epi = on, Taxi = arrangement. It is defined as the formation of a monocrystalline layer called (the epitaxial layer) on a monocrystalline substrate [36].

Molecular beam epitaxy is a method for developing thin films at low temperature with excellent crystalline quality and very low roughness in a very high vacuum ($<10^{-10}$ Torr). The principle of this technique (Figure I.10) is based on the reaction of atomic or molecular fluxes on a monocrystalline substrate which brought to an adequate temperature [37].

As shown in figure II.10, the growth process of the molecular beam epitaxy can be summarized in the following steps [37]:

1) Deposition of atoms onto the surface of the substrate

2) Nucleation process (creation of di-atomic islands)

3) Growth of islands by coalescence

4) Formation of a layer by coalescence of islands

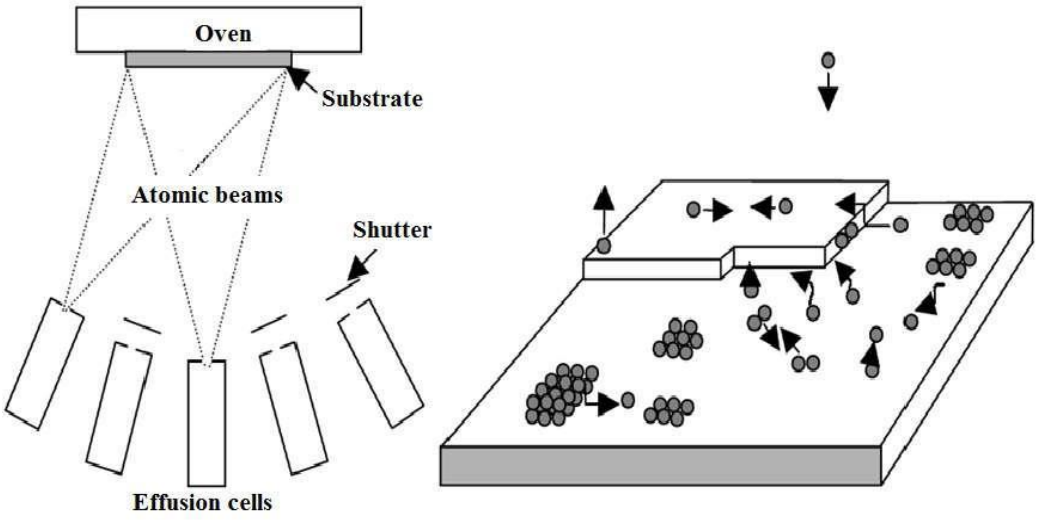

Figure I.10: The operating principle of MBE [37].

Molecular beam epitaxy has the following advantages [36]:

- The low growth rate that allows doping at the atomic level
- Possible controls and in situ analysis (RHEED; Auger XPS)
- Very precise control of the thicknesses of the thin layers
- The ability to control all the steps automatically
- No boundary layer.

c. Pulsed Laser Deposition

Pulsed Laser Deposition (PLD) is a deposition technique that has the advantage of transferring the stoichiometry of the target to the prepared layer, in this method a laser beam focused on a depositing material (target) placed in an ultrahigh vacuum chamber. Under the effect of this laser beam, an amount of the material is pulled away from the target in the form

of a dense and light vapor (plasma) and deposited on the substrate placed opposite as presented in figure I.11.

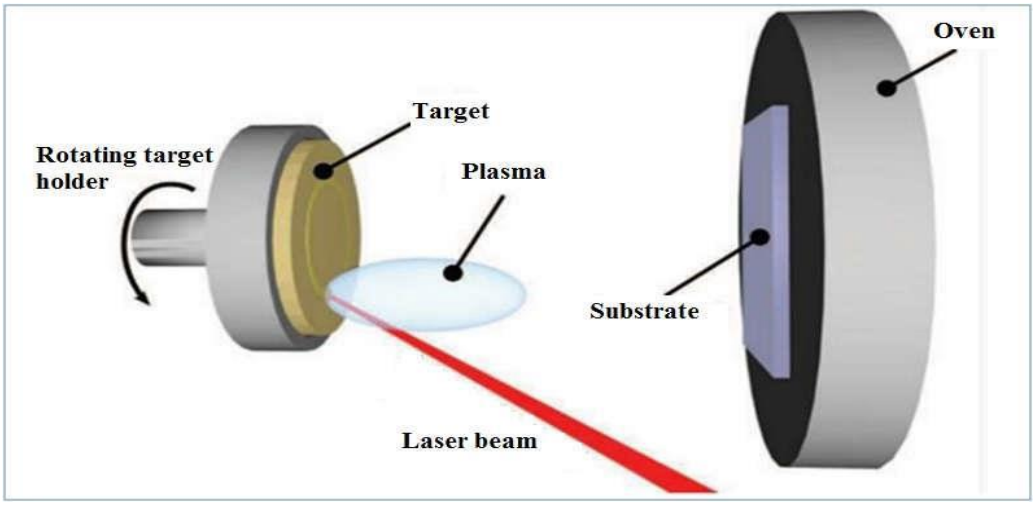

Figure I.11: Schematic diagram of the Pulsed Laser Deposition (PLD) technique [38].

Laser ablation has a number of advantages, it enables the deposition at room temperature and the coating of all types of the substrate [38], and it also allows the manufacture of the complex composition of materials in thin layers.

d. Thermal evaporation

The thermal evaporation process contains evaporating source materials in a vacuum chamber below 10^{-6} Torr and condensing the evaporated particles on a substrate. In this process, thermal energy is provided to a source from which atoms are evaporated for deposition in the substrate. Heating of the source material can be finished by any of which the material to be evaporated is attached. Larger volumes of source material can be heated in crucibles of refractory metals, Oxides or Carbon by resistance heating, high-frequency induction heating, or electron beam evaporation. The evaporated atoms travel through reduced background pressure in the evaporation chamber and condense on the growth surface. The deposition rate

or flux is a function of the travel distance from the source to the substrate, the angle of impingement onto the substrate surface, the substrate temperature Ts, and the base pressure. The conventional thermal evaporation system is mentioned in figure I.12 [39, 40].

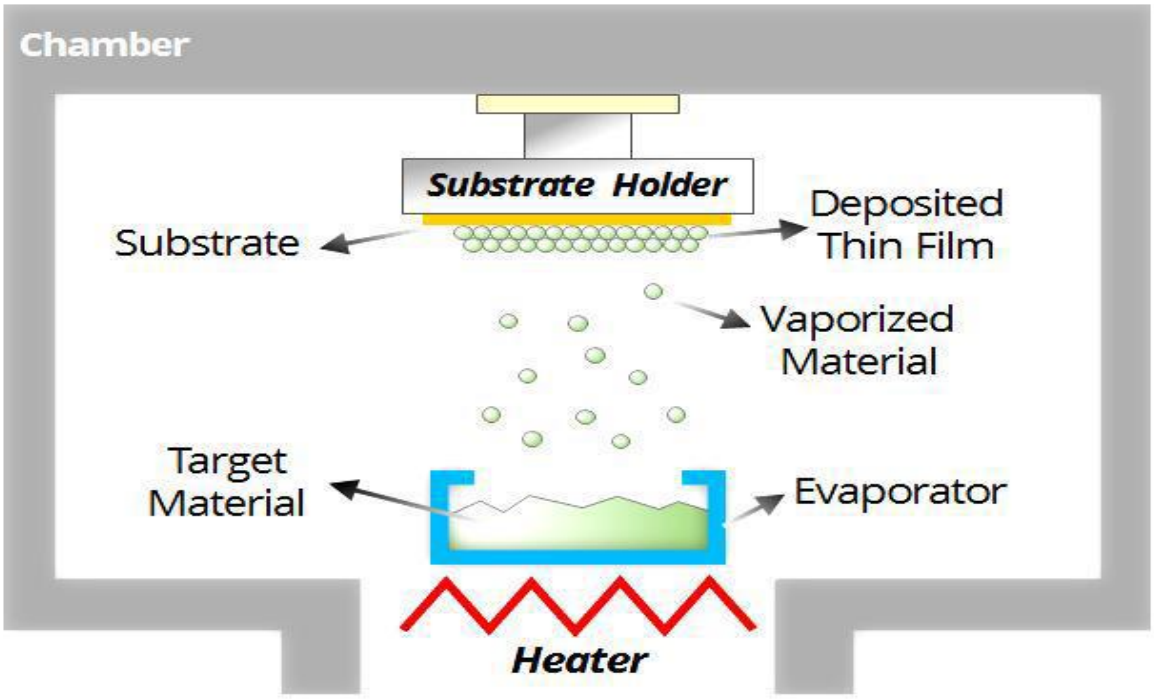

Figure I.12: Schematic diagram of thermal evaporation system [41].

I.1.8.2. Chemical deposition methods

a. Chemical vapor deposition (CVD)

The CVD technique consists of developing materials in the form of thin layers from gaseous precursors that chemically react to form these layers on a heated substrate [42], as shown in figure I.13. The CVD process can be summarized in five steps [37]:

- Transporting reactive gas species (or species) to the substrate.
- Adsorption of the reactants on the surface.
- Surface reaction and film growth.
- Desorption of volatile secondary products.

• Transport and evacuation of gaseous products to the reactor outlet.

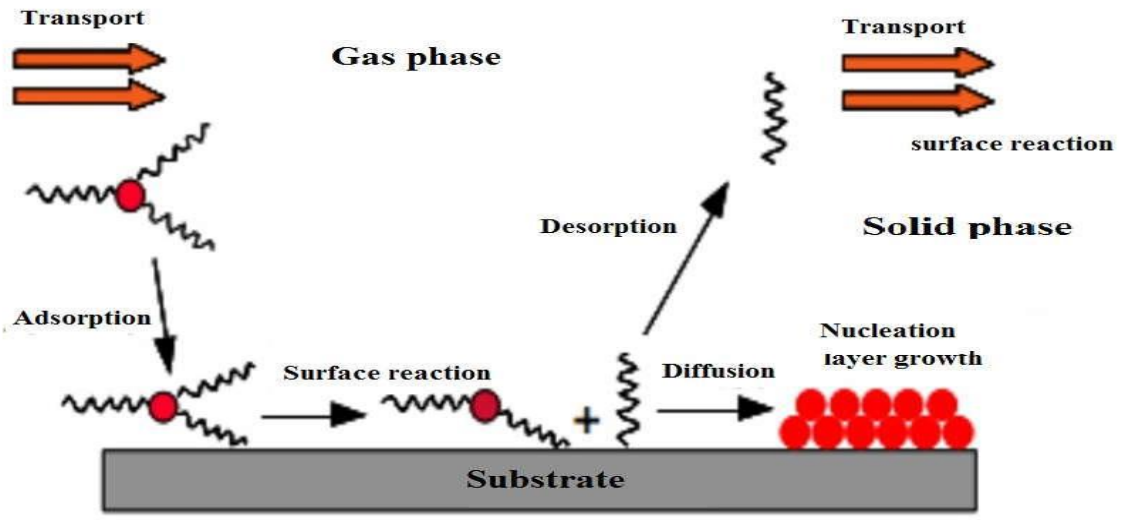

Figure I.13: Schematic diagram of thermal evaporation system [36].

The improvement of this technique is to reduce the deposition temperature and the reactor pressure and remedy the low volatility of the precursors. Several CVD type techniques can be given [43]:

• APCVD: (Atmospheric Pressure Chemical Vapor Deposition) deposition under atmospheric pressure.

• LPCVD: (Low-Pressure Chemical Vapor Deposition) low-pressure deposition.

• MOCVD: (Metal Organic CVD) the use of organometallic precursors.

• PACVD: (Plasma Assisted Chemical Vapor Deposition) with the assistance of a plasma.

b. Sol-gel

The term sol-gel corresponds to the abbreviation "solution-gelation". The sol-gel method (Figure I.14) used to manufacture various materials such as ceramics, powders, fibers, and thin films and is particularly well suited for producing coatings such as thin layers of oxides [44, 45]. Its principle is based on chemical reactions of a chemical precursor consisting of

metal atoms of the material that we want to deposit in a solution to form an oxide network at an infinite viscosity called "gel", depending on the nature of the precursors used. We distinguish two synthetic voices [46]:

Inorganic route: obtained from metal salts such as nitrates, sulfates, chlorides, or acetates; dissolved in an aqueous solution.

Organometallic route: The most frequently used precursor is metal alkoxides in organic solutions.

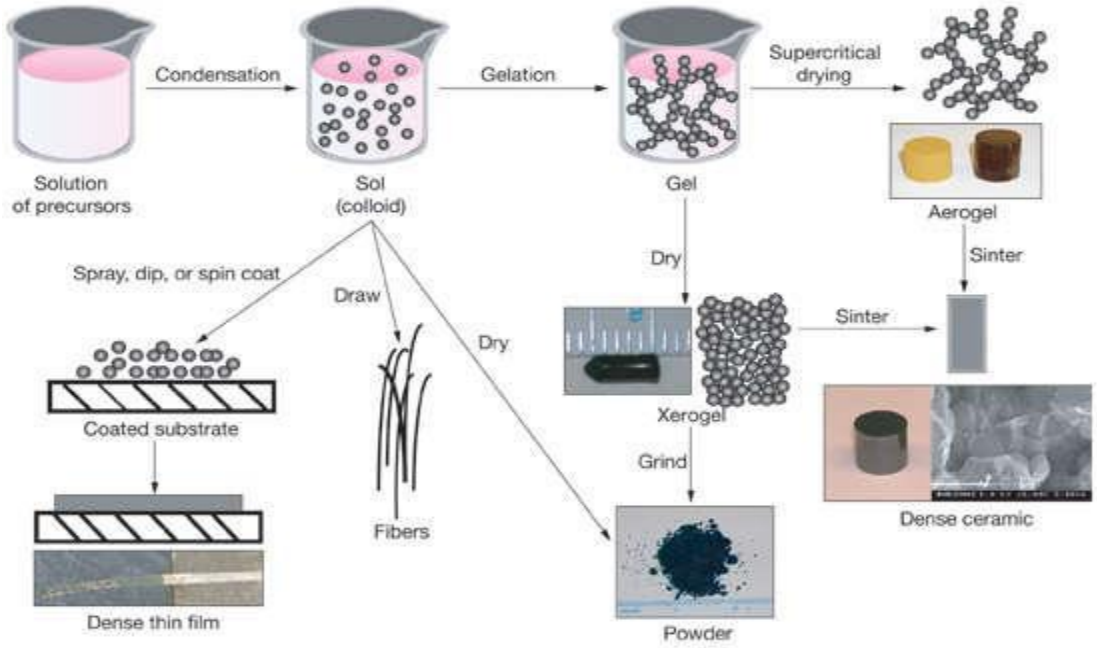

Figure I.14: Synthesis of various forms of materials by the sol-gel method [47].

c. Chemical bath deposition

The chemical bath deposition (CBD) is also recognized as controlled precipitation; it has been applied since to deposit films of many different semiconductors. It is currently attracting great attention as it does not necessitate sophisticated instrumentation like vacuum system and other expensive equipment. All that is required is a vessel to include the solution (an aqueous solution made up of a few usually common, chemicals) and a substrate on which deposition is

required. It offers a bottom-up approach to prepare nano-crystalline materials in thin film form with better particle size controlled, particle shape, size distribution, particle composition, the degree of particle agglomeration, the conventional thermal evaporation system is presented in figure I.15 [48].

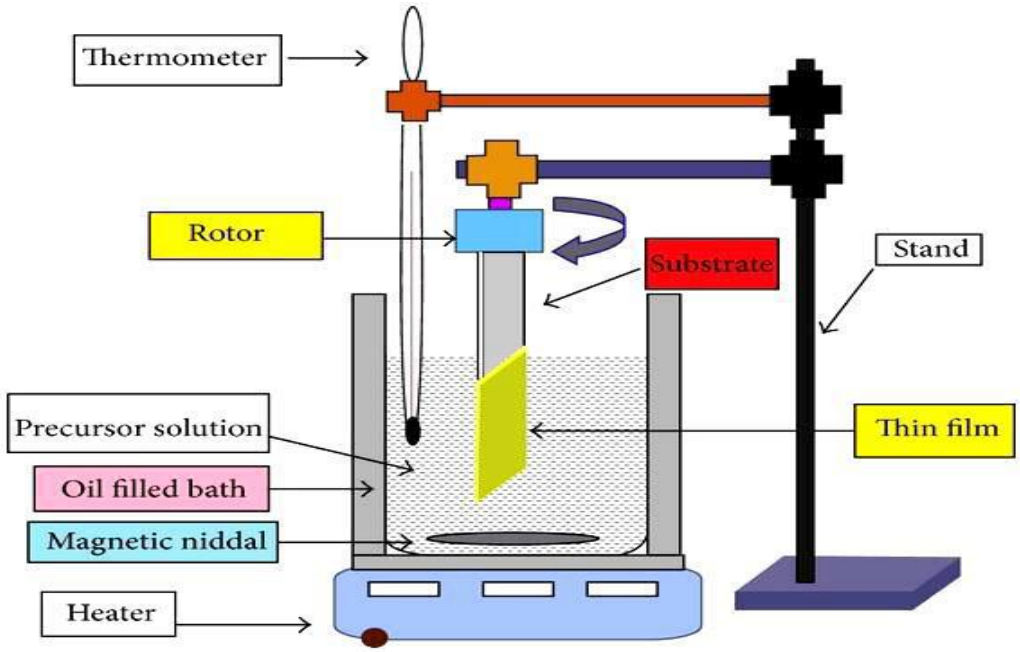

Figure I.15: Schematic diagram of chemical bath deposition system [48].

I.2. Barium tin oxide compounds (Ba-Sn-O system)

Because of their novel and interesting functional properties, perovskite oxides ABO_3 such as $BaSnO_3$ and anti-perovskite oxides A_3BO such as Ba_3SnO, became an important class of materials by attracting attention of many researchers for their remarkable physical properties [49-51]. These oxides illustrate insulating, metallic, semiconducting and superconducting materials behavior [52], which offered them possible applications in many fields such as thermal devices [53], photovoltaic solar cells [54] and gas sensors [55].

I.2.1. ABO_3 perovskite oxides

Metal oxides are a group of earth-abundant materials that display properties relevant to numerous technological applications. Depending on the number of components, these oxides can range from simple binary oxides, such as ZnO, to more complex ternary and quaternary formulations containing multiple cations. A particular class of complex metal oxides that have generated much attention over the past few decades are the perovskites [56].

I.2.1.1. History of perovskite

Originally, the term "perovskite" was used to denote a specific mineral, the calcium titanate $CaTiO_3$, called perovskite in honor of Lev.Aleksevich.von Perovski (1792, 1856) Russian mineralogist, by Gustav Rose who first discovered it in 1839 from samples found in the Ural Mountains. The name perovskite is commonly used to designate a group of materials that have a crystalline structure related to that of $CaTiO_3$. See figure I.16.

Figure I.16: Lev Aleksevich von Perovski and the perovskite mineral species ($CaTiO_3$) [57].

I.2.1.2. Perovskite oxides structure

Perovskite oxides have a general chemical formula of ABO_3 and crystallize in a cubic structure as shown in figure I.17 (a). Although this cubic representation is an

oversimplification for most perovskite crystals, it is useful in depicting the three ionic sites in the unit cell: corners represent the A site, the body center represents the B site, and the face centers are occupied by oxygen. The six oxygen ions surrounding the B site cation form an octahedral cage, and the crystal structure in Figure I.17(a) can be equivalently visualized as a three-dimensional network of corner-shared BO_6 octahedra, as shown in figure I.17(b) [56].

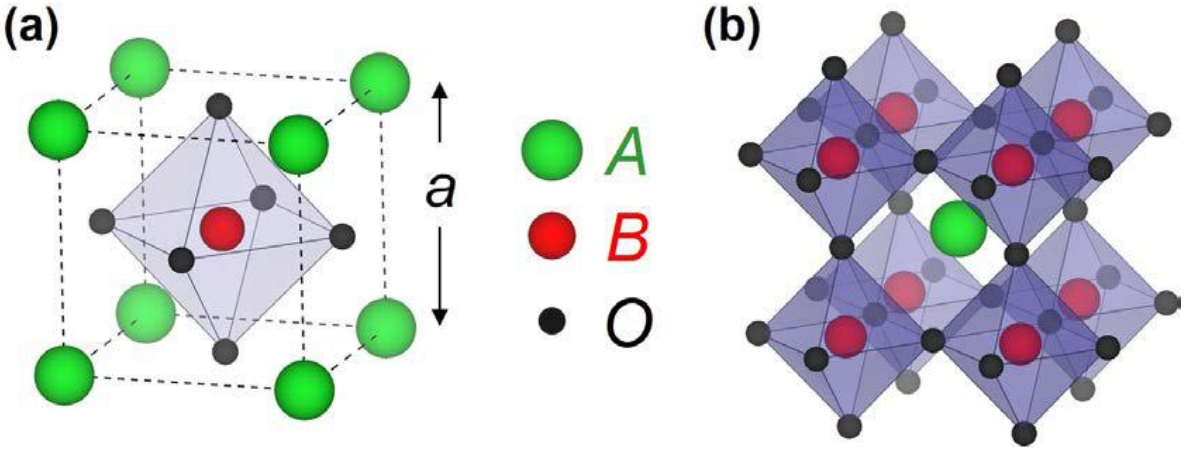

Figure I.17: (a) The perovskite unit cell showing the positions of the *A* site, *B* site, and oxygen. (b) An alternate presentation of the same crystal showing a three-dimensional network of corner shared BO_6 octahedra [56].

I.2.1.3.Deviations from ideality

Assuming the ions are rigid spheres that touch along the edge and face diagonal of the cube in figure I.17 (a), the lattice parameter, *a*, can be related to the ionic radii of the A, B, and O ions (R_A, R_B, and R_O, respectively) through simple geometry as:

$$2(R_A+R_O) = \sqrt{2}a \quad \text{and} \quad 2(R_B+R_O) = a \qquad \text{(I.1)}$$

The above equalities both hold true only for an ideal cubic unit cell. In general, a Goldschmidt tolerance factor, *t*, is used to quantify deviations from the ideal cubic structure and is defined by:

$$t = \frac{R_A + R_O}{\sqrt{2}(R_B + R_O)} \qquad \text{(I.2)}$$

Comparing Eqs.I.1 and I.2, it becomes clear that t = 1 for the cubic crystal structure. Surprisingly, the perovskite structure is extremely amenable to variations in the ionic radii of the A and B cations, thus resulting in t values in the range of 0.89 – 1.02. This variation in t is accommodated through tilting and distortion of the BO_6 octahedra, and is accompanied by displacements of the cations and changes in the B–O–B bond angle [56] (Figure I.18). This lowers the crystal symmetry from cubic to tetragonal, rhombohedral, orthorhombic, monoclinic and triclinic [58, 59].

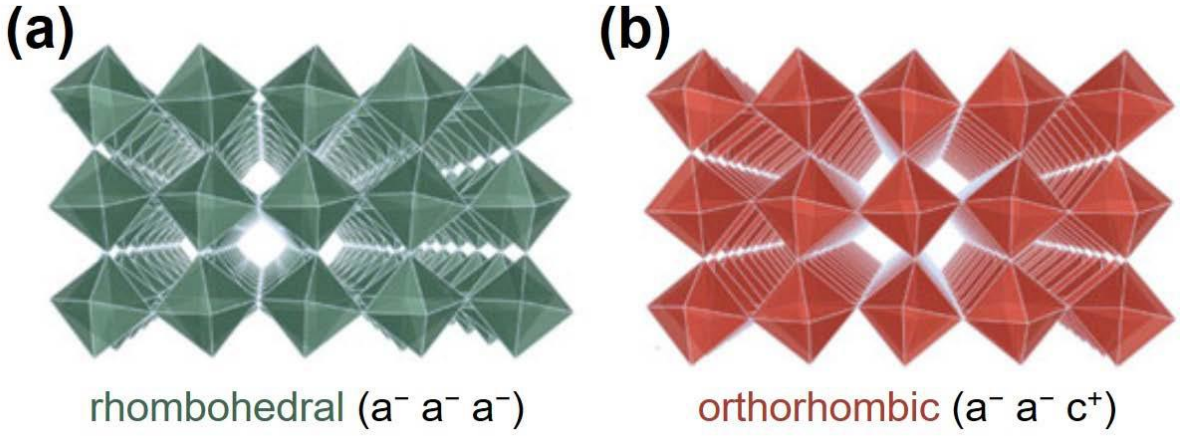

Figure I.18: Schematic illustration of the BO6 octahedral tilting in perovskite oxides with (a) rhombohedral, and (b) orthorhombic crystal structures. The rotational patterns are also indicated. Figure adapted from [59].

I.2.1.4. Stoichiometric aspects of the perovskite structure

For simple ABO3 oxide systems, the following classification can be made, based on cationic valences:

[1 + 5] = A1B5O3

[2 + 4] = A2B4O3

[3 + 3] = A3B3O3

Only these three types cover a wide range of compounds. However, a large number of other possibilities arise when we consider mixed cation structures of the type: A1+xA′ xBO3.
The following are also possible: AB1+xB′xO3, A1+xA′ xB1+yB′y O3, A2BB′O9, etc... [60].

I.2.1.5.Defects in perovskite structure

Due to their exible structure, perovskite oxides can adapt to a combination of cation oxidation states if the charge neutrality condition is satisfied (sum of the oxidation states for cations = 6). Further modifications to the crystal and electronic structures of perovskite oxides can be achieved by alloying (isovalent substitution) or doping (aliovalent substitution) at the A or B sites. Structural changes are discernible in oxides when they are alloyed above a certain limit due to changes in the tolerance factor [61].

Doping concentrations, on the other hand, are usually smaller to cause global structural changes. Aliovalent substitution introduces extra electrons or holes in the lattice resulting in noticeable changes to the electronic structure. Depending on whether the dopant acts as an acceptor or donor, p-type (hole) or n-type (electron) carrier transport can be observed, respectively. For instance, in $SrTiO_3$, p-type conduction is observed if it is doped with Sc on the B site, whereas La doping at A site results in n-type transport [62, 63].

I.2.1.6. Physical properties of perovskite oxides

The perovskite oxide has continuously attracted attention because the members contain an extensive range of materials properties. All three common electronic states, metals, insulators, and semiconductors, have been observed in the perovskite family. There are also rich physics and engineering opportunities in these materials. For example, $SrTiO_3$ is found to have ferroelectricity and superconductivity [64, 65], and $BaSnO_3$ has been considered as a great candidate as a next-generation transparent conducting oxide [66, 67]. The differences in properties of the perovskite family members are associated with different combinations of A and B cations, despite the perovskites all sharing the same general crystal structure [68].

Figure I.19 (a) shows the elements from the periodic table that can fill the A and B sites without destabilizing the perovskite lattice. Thus, Owing to the staggeringly large number of A and B cation combinations, perovskite oxides display a myriad of diverse functionalities (Figure I.19 (b)).

I.2.1.7. $BaSnO_3$ perovskite oxides

Oxide materials with the perovskite structure have exhibited a plethora of interesting physical properties, such as large photovoltaic effects [69, 70], ferroelectricity and superconductivity [64, 65]. $BaSnO_3$ is one of the perovskite oxides that have brought attentions for optoelectronic devices due to its high electron mobility, high transparency, wide band gap and flexible doping controllability.

a. Crystal structure of $BaSnO_3$

There exist three compounds in the $BaO–SnO_2$ binary system, $BaSnO_3$, $Ba_3Sn_2O_7$ and Ba_2SnO_4, but barium stannate or barium tin oxide is normally referred to as $BaSnO_3$ because $BaSnO_3$ is the best known among these, the most thoroughly investigated and the most useful compound. Barium tin oxide ($BaSnO_3$) belongs to the perovskite oxide compounds. $BaSnO_3$

crystallizes in a cubic perovskite structure as shown in the figure I.20. In this cubic structure, the Ba^{2+} ions (1.34 Å) occupy the corners of the unit cell, the Sn^{4+} ions (0.71Å), the volume center, and the O^{2-} ions (1.40 Å), the surface center. In this structure, the larger Ba^{+2} ions and the O^{-2} ions build a cubic, dense, ball by packing together.

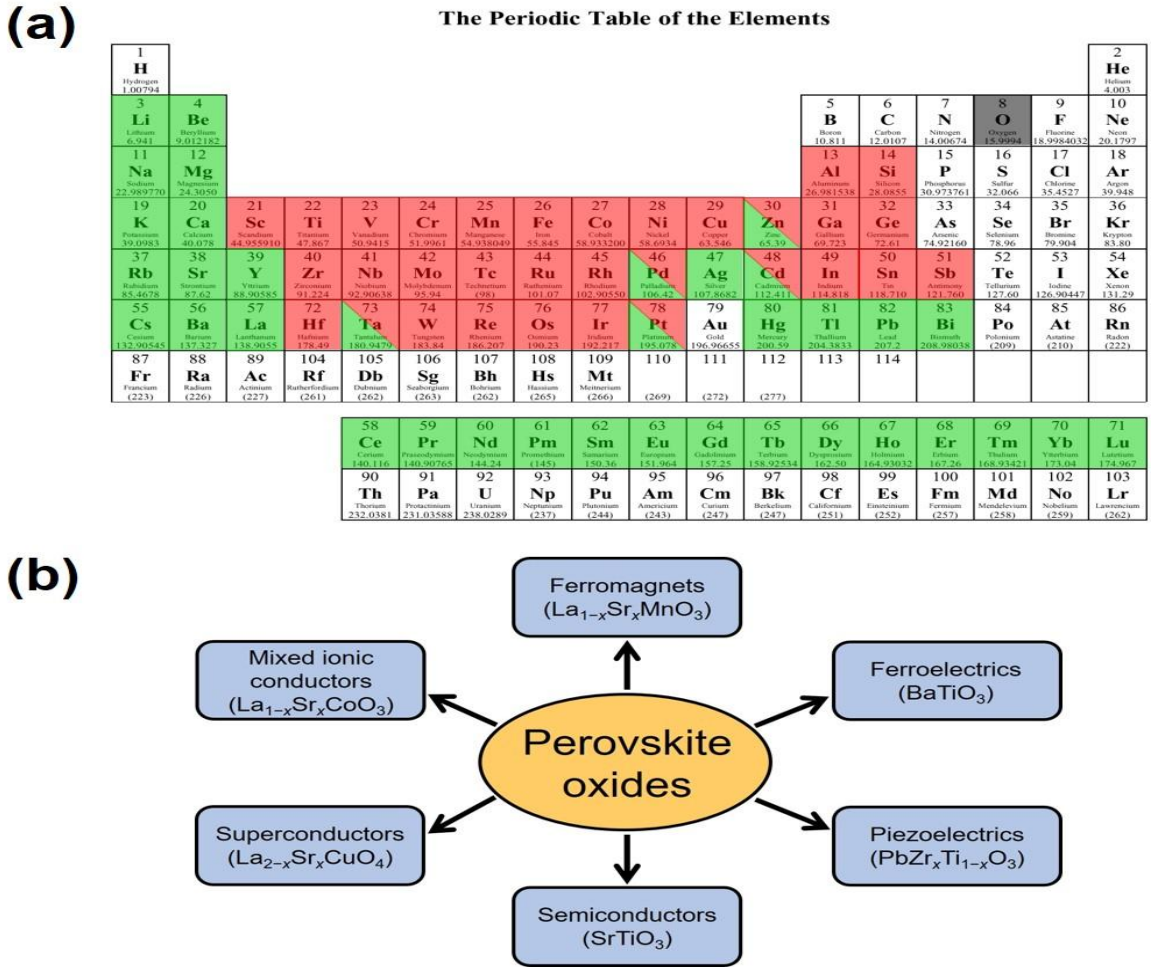

Figure I.19: (a) The periodic table highlighting the elements that can be incorporated into the perovskite structure. Elements shaded in green can go into the *A* site, while those in red can go into the *B* site. (b) Diverse functionalities of perovskite oxides and their derived structures [56].

A quarter of the octahedral holes is filled with small Sn^{4+}ions. Each Ba^{2+}ion is coordinated with 12 O^{2-} ions and each O^{2-} ion is surrounded by four Ba^{2+} ions and two Sn^{4+} ions. Thus, the

crystallochemical formula is Ba $^{[12]}$ Sn $^{[6]}$ O3 $^{[4+2]}$. The octahedrons of [SnO_6] are linked by sharing corners to form a three-dimensional framework as illustrated in figure I.20 [71].

Goldschmidt tolerance factor, according to Shannon's ionic radii, equals to t=1.02 [72]. Its value shows that the structure theoretically has no polar distortions and is probably too high to have SnO_6 octahedral tilts in the lattice. $BaSnO_3$ space group in Hermann Maugain system is *Pm*-3*m* (221). Its lattice parameter *a* of 4.117 Å [73, 74] was determined experimentally and theoretically [75, 76] and reported in various papers. $BaSnO_3$ has a lattice volume of 73.5 Å.

It should be understood that this high-symmetry cubic structure can distort and deform under specific conditions so that the structure symmetry degree is lowered [71].

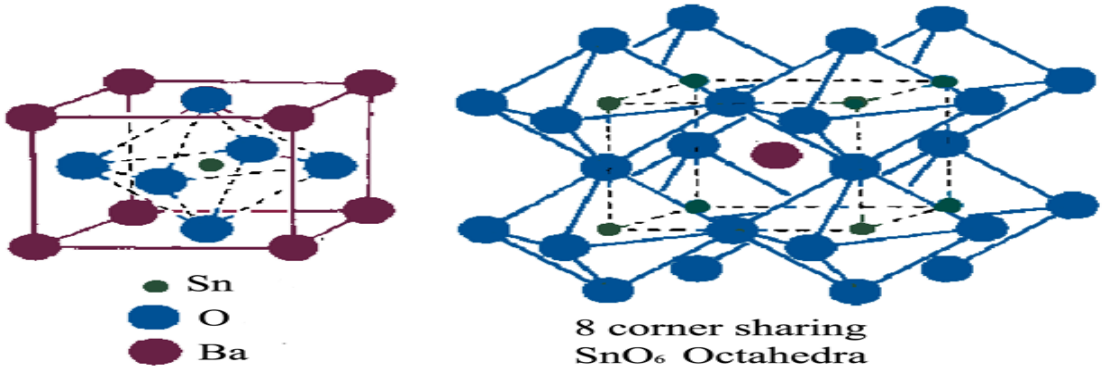

Figure I.20: $BaSnO_3$ perovskite structure.

b. Electronic Band structure of $BaSnO_3$

In the $BaSnO_3$ structure, the electronic valence configuration for each atomic species corresponds to Ba: $5s^2 5p^6 6s^2$, Sn: $4d^{10} 5s^2 5p^2$, and O: $2s^2 2p^4$.

Band structure calculations on $BaSnO_3$ have revealed that the conduction band minimum (CBM) and valence band maximum (VBM) are positioned at the Γ and R points in reciprocal space [77-79], respectively, as shown in figure I.21, indicating $BaSnO_3$ as an indirect band gap materials. A wide indirect band gap of $Eg \approx 3$ eV results in a visible transmittance ~80%

[80, 81]. The CBM is dominated by Sn-5*s* states, resulting in an increased dispersion of the CB, and in turn, a relatively small effective mass [56].

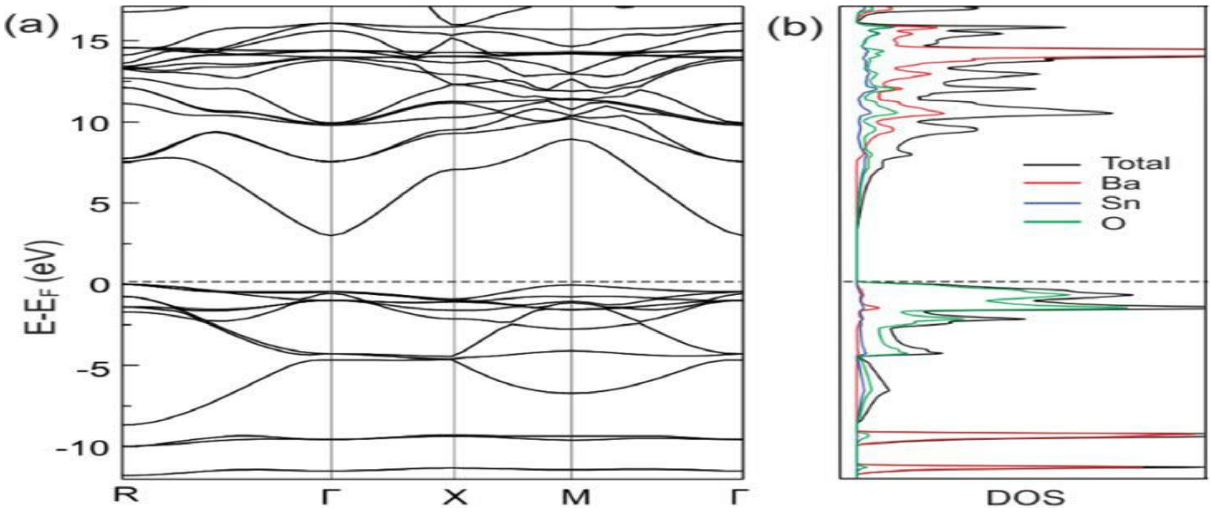

Figure I.21: (a) Calculated band structure and (b) corresponding density of states (DOS) of BSO. Figure adapted from [77].

c. Electrical properties of $BaSnO_3$

$BaSnO_3$ has emerged as one of the potential candidates for transparent conducting oxides with room-temperature conductivity exceeding 1.0×10^4 S cm^{-1} [80, 83]. Figure I.22 summarizes room-temperature electron mobility as a function of carrier density in $BaSnO_3$ single crystals as well as thin films. Interests in $BaSnO_3$ as a potential candidate for transparent conductors were generated by the discovery of high room-temperature mobility in single crystals of La-doped $BaSnO_3$ by Luo et al. when they reported electron mobilities above 100 cm^2 V^{-1} s^{-1} at a carrier concentration of 1.0×10^{20} cm^{-3} and a wide direct band gap of 4.0 eV [84]. Later, Kim et al. showed that mobility in La-doped $BaSnO_3$ single crystals can reach as high as 320 cm^2 V^{-1} s^{-1} at a carrier concentration of 8.0×10^{19} cm^{-3} [85].

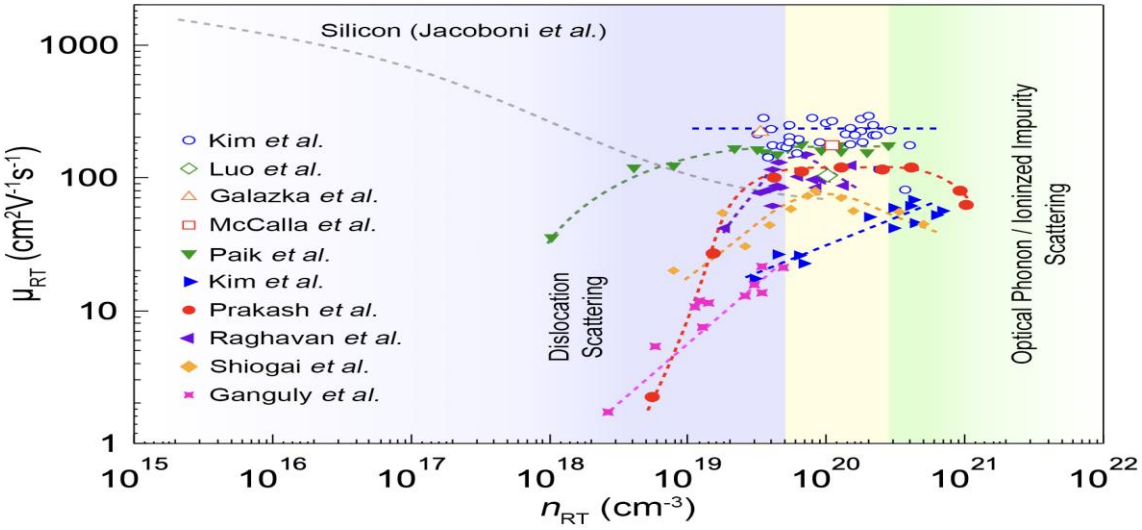

Figure I.22: Room-temperature electron mobility in single crystals and epitaxial thin films of doped $BaSnO_3$. Data were taken from ref. [82-91].

High room-temperature electron mobility in doped $BaSnO_3$ is usually attributed to low electron-phonon scattering and small electron effective mass (m_e). The conduction band minima in $BaSnO_3$ is derived predominantly from a more dispersed Sn -5s state which results in a small m_e [92]. A wide range of electron effective mass between 0.06 m_0 - 0.6 m_0 (m_0 is the rest mass of an electron) have been reported through experiments and theoretical calculations for $BaSnO_3$ [83, 93, 94]. However, recently this number has been shown to converge towards 0.2 m_0 [95, 96], which is comparable to the electron effective mass of other transparent conductors such as ZnO, In_2O_3, and SnO_2.

d. Optical properties of $BaSnO_3$

Besides having high room-temperature mobility, $BaSnO_3$ also has a wide indirect band gap experimentally determined to be in the range of 2.9 - 3.2 eV [97, 98], which makes it optically transparent. Although theory is prone to underestimate the band gaps, Tran-Blaha modified Becke-Johnson (TB-mBJ) and Perdew-Burke-Ernzerhof density functionals predict indirect

band gaps of 2.8 eV [92,99]. Compared to $SrSnO_3$ and $CaSnO_3$, the Sn-O-Sn bond angle in $BaSnO_3$ is exactly 180°. This leads to a smaller overlap between Sn-5s and O -2p orbitals and hence smaller band gap in comparison to $SrSnO_3$ and $CaSnO_3$ that have band gaps in the range of 4 - 5 eV [61].

e. Chemical Doping in $BaSnO_3$

$BaSnO_3$ can be doped by chemical substitution on either the A (Ba) or B (Sn) sites. While p-type doping has proved to be extremely challenging, *n*-type doping has commonly been achieved through La^{3+} substitution for Ba^{2+} and Sb^{5+} substitution for Sn^{4+}. By far the most widely studied doping has been the substitution of Ba by La (La_{Ba}). Lanthanum, like most rare earth elements, forms a stable +3 cation, and as such it acts as an electron donor in $BaSnO_3$.

The electrons donated by La^{3+} occupy these empty antibonding states and hence result in repulsive forces between Sn and O leading to a lattice expansion [100]. Liu *et al.* predicted the La donor level to be very shallow (≈50 meV below the CB) in $BaSnO_3$ [101] and, indeed, both $Ba_{1-x}La_xSnO_3$ (BSO: La) single crystals and thin films exhibit degenerate metallic conduction starting at a low dopant concentration (x) [56].

f. Application of BaSnO3 perovskite oxides

High optical transparency, wide band gap and good electrical conductivity in doped $BaSnO_3$ have prompted researchers to theoretically and experimentally explore this material as a potential transparent conducting oxide (TCO).

Among various applications using the advantages of wide band gap $BaSnO_3$ (BSO), fully solidified perovskite solar cell is recently investigated using BLSO as an electron transporting layer (ETL) [102]. A solar cell (Figure I.23 (a)), is an electrical device, converting the energy

of light into electricity, appealing as a renewable energy generation and storage devices for new generation. As illustrated in figure I.23 (b), the created electron-hole pair by sunlight moves to each end metal contact to generate current through external load. Because usual metal electrodes are opaque, reducing power conversion efficiency (PCE) in solar cell, TCOs such as In_2O_3: Sn [103], SnO_2 [104], ZnO [105] are appropriate, having both transparency and conductivity. Usual solar cells use Si pn-junction to make electron-hole pair, but perovskite materials based on lead halide ($CH_3NH_3PbX_3$; X is I and Br) as dyes have shown remarkable increase of PCE, appealing as an important candidate for photovoltaic devices [106, 107]. In figure I.23 (c), the superior performance of perovskite solar cell fabricated with BLSO as an ETL is presented in photocurrent density-voltage (*J*-*V*) characteristics and compared with mesoporous TiO_2, which is a typical ETL for highly efficient perovskite solar cell. The PCE is 21.2 % for using BLSO as a TCO and 19.7 % for TiO_2, which is attributed by higher conduction band minimum, higher electron density, and reduced carrier recombination. And experiment for photostability under light illumination describes a greater resistance against photodegradation than TiO_2 in figure I.23 (d), making closer to a commercialization of perovskite solar cell [108].

Apart from the transparent electronics using its wide band gap of BSO, another potential area will be high temperature and power electronics [109]. Wide band gap semiconductors (WBGs) can perform in a high temperature without losing their electrical property due to its wide band gap, so it can function at ambient temperature without external cooling, beneficial for the automotive, aerospace, and energy production industries. Moreover, its high breakdown voltage makes higher doping levels achievable and higher saturation drift velocity makes possible to operate at higher switching frequency. In turn, the lower conduction loss and lower switching loss can enable breaking the limit of silicon-based power electronics, e.g. radio-frequency application and energy production like photovoltaic inverter technology.

Already WBGs such as SiC and GaN are commercially available, so BSO can go beyond TCO, if much effort to achieve higher efficiency for high temperature and power device requirement are done. [108].

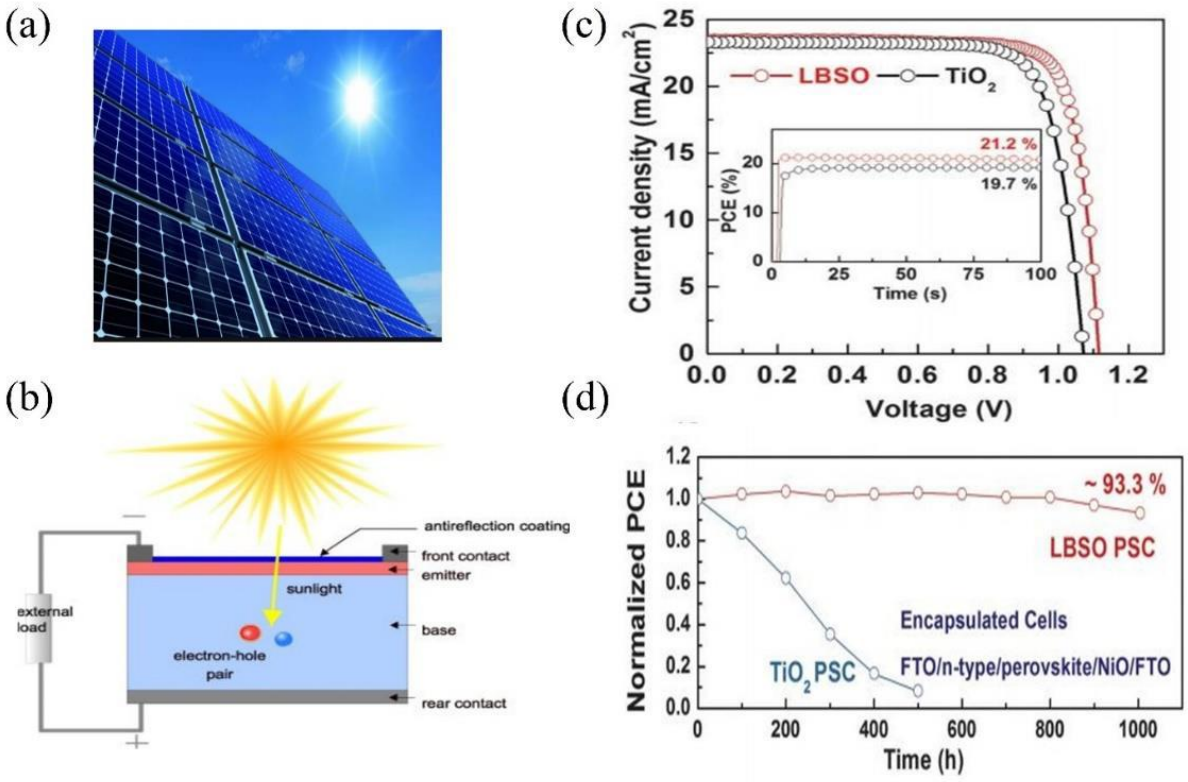

Figure 1.23: Application for solar cell (a) Solar panels. (b) Cross section of solar cell (c) J-V curves and PCEs at a maximum power point for the best performing BLSO and TiO_2 based perovskite solar cell. (d) Long term photostability test under AM 1.5G illumination with a metal-halide lamp, including UV radiation for BLSO and TiO_2-based perovskite solar cell [108].

I.2.2.A_3BO anti-perovskite oxides

Anti-perovskites are the counterparts of perovskites. They have diverse properties that make them physically rich and technologically relevant. In the recent years, Ba_3SnO anti-perovskite oxides, with small semiconductor band gap, have captured tremendous attention due to their

properties which make them efficient to be used in optoelectronic, photovoltaic conversion devices.

I.2.2.1.Crystal structure of anti-perovskite oxides

Generally, the perovskite oxides are symbolized by the formula ABO_3. If the position of A and O are exchanged, then the new resultant class of material is formed which is called anti-perovskite oxides which have cubic structure. Then the general formula for anti-perovskite is A_3BO. In this structure, The "B" atoms occupy the corner of the cubic lattice, "O" and "A" atoms are located at the body-centered and the face-centered of the lattice, respectively. Wyckoff atomic positions are: B: 1a (0, 0, 0); O: 1b (1/2, 1/2, 1/2); A: 3c (1/2, 1/2, 0). Thus, in anti-perovskite unit cell, the "O" atom is surrounded by six "A" atoms to form an octahedral cage generating a three-dimensional network of A_6O octahedrons, while the B atom is coordinated cuboctahedrally with twelve A atoms (Figure I.24).

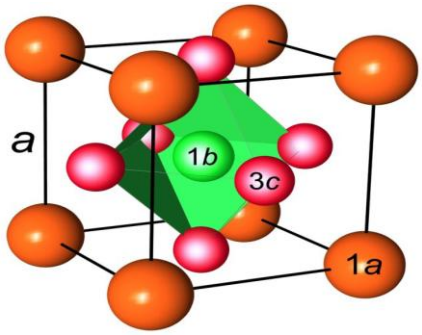

Figure I.24: Crystal structure of anti-perovskite oxide [110].

I.2.2.2.Physical properties of anti-perovskite oxides

Similar to the perovskites, anti-perovskite seek the considerable attention of both the theoreticians and the experimentalists because of their appealing technological applications.

The anti-perovskite unveil an extensive range of innovative phenomena like giant magnetoresistance (GMR) magneto-volume effect (MVE) [111], zero temperature coefficient of resistivity [112], negative thermal expansion [113], superconductivity [114] and magnetostriction [115]. In addition, they also reveal the semiconducting [116] and insulating properties [117].

Anti-perovskite oxides A_3BO (A = Mg, Ca, Sr, Ba, Eu, Yb and B = Si, Ge, Sn, Pb)) have recently been demonstrated to exhibit Dirac electronic dispersion near the Γ point in the Brillouin zone based on first-principles calculations . They have the perovskite crystal structure but with O^{-2} ions occupying the center of the octahedron formed by A^{+2} ions. To satisfy the charge-neutrality relation, the B ions, Sn in Sr_3SnO, take an unusual 4- oxidation state and, as a consequence, their p orbitals are almost filled [118, 119]. This unusual electronic configuration can lead to interesting properties. Indeed, theoretical works on Ca_3PbO predicted a 3D Dirac dispersion in the electronic band [120, 121]. This Dirac dispersion originates from the band inversion of the empty Ca-3d and filled Pb-6p bands near the Γ point, as well as from the avoided hybridization between these bands due to crystal symmetry.

The Dirac point has a small gap in the order of ≈10 meV [120], due to higher-order interactions originating from the spin-orbit coupling. This gapped state was later predicted to be a topological cryrstalline insulator state [122].

I.2.2.3. Ba_3SnO anti-perovskite oxides

The anti-perovskites materials have been an interesting research topic due to their various applications in several fields like in electronics and optoelectronics. In this work, we are shading light on the Ba_3SnO anti-perovskite due to its narrow band gap. Thus, it can be considered as a promising candidate for optoelectronic applications.

a. Crystal structure of Ba_3SnO

Ba_3Sno crystallizes in the cubic anti-perovskite-type structure as shown in the figure I.25. The "Sn" atoms occupy the corner of the cubic lattice, "O" and "Ba" atoms are located at the body-centered and the face-centered of the lattice, respectively. Wyckoff atomic positions are: Sn: 1a (0, 0, 0); O: 1b (1/2, 1/2, 1/2); Ba: 3c (1/2, 1/2, 0). Consequently, in anti-perovskite BSO unit cell, the "O" atom is surrounded by six "Ba" atoms to form an octahedral cage generating a three-dimensional network of Ba_6O octahedrons, while the Sn atom is coordinated cuboctahedrally with twelve Ba atoms. Its lattice parameter *a* is 5.51 Å [117].

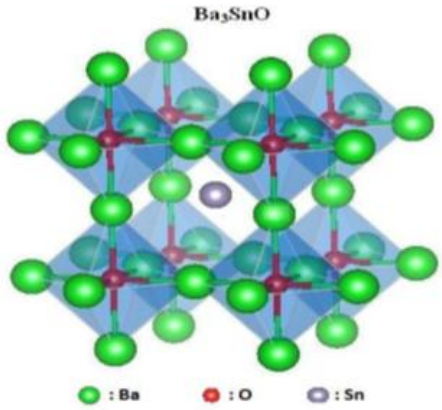

Figure I.25: Cubic structure of Ba_3SnO anti-perovskite oxide [123].

In Ba_3SnO anti-perovskite oxides, one can expect the ionic configuration $(Ba^{2+})_3\,Sn^{4-}O^{2-}$ with a metallic Sn anion. The metallic Sn anion takes a formal 4- valence state to keep charge neutrality, which is unusual for a metal element [123].

b. Electronic band structure of Ba_3SnO

The band structure computed by using mBJ functional for anti-perovskite Ba_3SnO is shown in figure I.26. As is evident in this figure , the Fermi level (taken at 0.0 eV) appear close to the valence band .The conduction band minima for Ba_3SnO are located at the Γ point, while the

valence band maxima also occur at Γ point, which reveal that these compounds exhibit (Γ-Γ) direct band gap. The narrow band gaps Eg = 0.10885eV extracted for Ba_3SnO make them remarkably useful for technological applications [117].

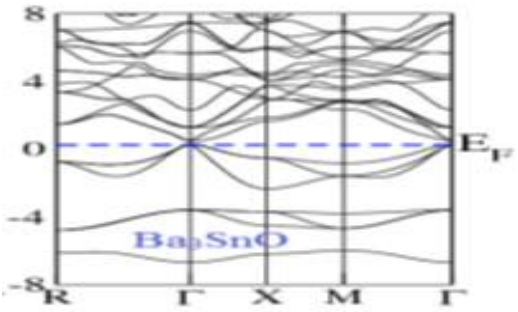

Figure I.26: The band structure of Ba_3SnO determined by applying PBE-mBJ potential [117].

The figure I.27 illustrate the calculated total (TDOS) and the partial density of states (PDOS) elucidating contributions from various constituents states of Ba_3SnO. The p-p hybridization can be seen on the PDOS above Fermi level. The Sn-5p and O-2p are strongly hybridized with a minor contribution from Ba-4s states, which suggest the presence of covalent bonding [124].

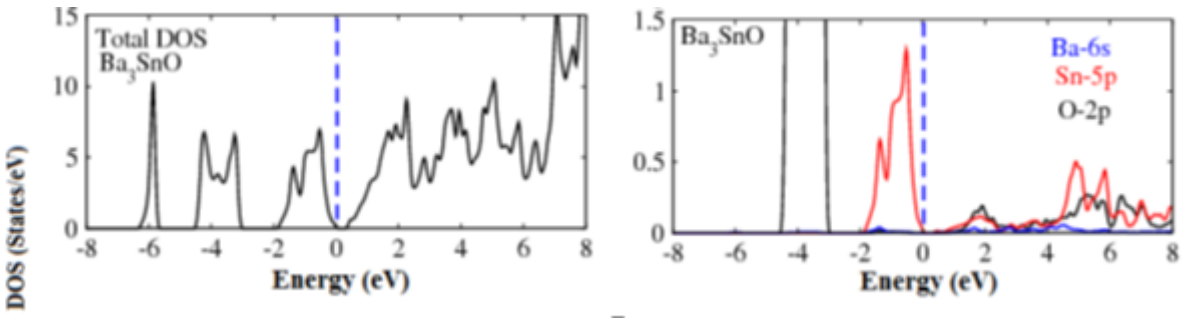

Figure I.27: The density of states (total and partial) computed by applying PBE-mBJ potential [117].

c. Electrical properties of Ba_3SnO

The small band gap of Ba_3SnO Eg = 0.10885eV [117] intensifies the carrier mobility. Ba_3SnO (BSO) is predicted to be a topological semimetal exhibiting twin Dirac cones near the Fermi level [125]. The low-energy electrons in topological semimetals are quite interesting since they show very high mobilities due to the linear dispersion character of the corresponding electronic states [126, 127].

The emergence of band dispersion in Ba_3SnO [128] leading to the formation of Dirac cone at the Fermi level .The emergence of Dirac point in the vicinity of Fermi energy confirms the presence of Dirac electrons which can easily cross the valence band leading to enhanced carrier mobility [129].

Recent experiments employing molecular beam epitaxy (MBE) and pulsed laser deposition (PLD) techniques for the synthesis of A_3SnO (A= Ca, Ba, Sr) thin films on various substrates indicate that (001)-oriented surfaces are experimentally achieved showing metallic character [130-132].

c. Optical properties of Ba_3SnO

The absorption of incident radiations leads to the electronic shifts from the VB to the CB to form the optical response of a material. Therefore, the optical properties of cubic Ba_3SnO are related to their band structures and play an important role to understand the technological and industrial applications. Ba_3SnO reveals direct (Γ-Γ) and narrow band gap nature, which is an attractive material property for optical applications [117].

Hassan and his co-workers [117] reported that the maximum absorption exhibited within 3.4eV and the maximum reflectivity at 4.8eV demonstrate significance of Ba_3SnO anti-perovskite oxides for optoelectronic device applications.

f. Application of Ba_3SnO anti-perovskite oxides

The anti-perovskite A_3SnX (X = C, N or O) have attracted huge interests due to various potential applications such as the transparent conducting oxide [133], novel chemical sensors [134], water photoelectrolysis [135, 136], antistatic thin layer [137] and the flat panel displays [138] etc. The anti-perovskites of carbide and nitride have been extensively studied but the family of oxides such as Ca_3SnO [139], Mn_3SnO [140] and Ba_3SnO [14, 15] have been less investigated [117]. The A_3SnO (A= Ca, Ba, Sr) exhibit narrow direct band gap. The transparency and maximum reflectivity to the certain energies of it indicate potential optical device applications [117].

Chapter II

Experimental procedures

In the first section of this chapter, we describe the chemical spray pyrolysis deposition method which has been chosen for preparation of both barium–calcium tin oxide and barium lead-tin oxide thin films. The deposition parameters of these thin films by this method will be also presented. In the second section, we describe the different characterization techniques used to study the effect of the substitution of barium by calcium and the substitution of tin by lead on structural, optical and luminescence properties of deposited films.

II.1.Chemical spray pyrolysis technique

II.1.1. Principle of the spray process

Spray pyrolysis is a processing technique being considered in research to prepare thin and thick films, ceramic coatings, and powders. The method has been employed for the deposition of dense films, porous films, and for powder production. Even multilayered films can be easily prepared using this versatile technique. Spray pyrolysis has been used for several decades in the glass industry [141] and in solar cell production to deposit electrically conducting electrodes [142].

Spray pyrolysis is a process where a precursor solution, containing the constituent elements of the compound, is pulverized in the form of tiny droplets onto the preheated substrate, where upon the thermal decomposition of the precursor an adherent film of thermally more stable compound forms [143].

Typical spray pyrolysis equipment consists of an atomizer, precursor solution, substrate heater, and temperature controller [144]. Figure II.1 shows the schematic representation of spray pyrolysis.

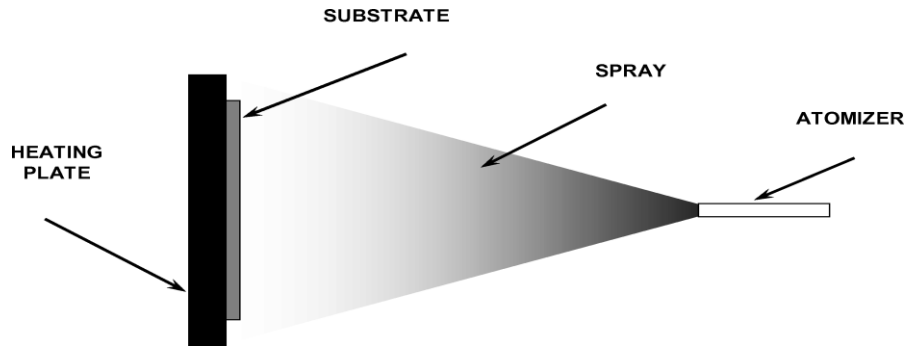

Figure II.1: Schematic representation of spray pyrolysis.

The description of the film formation by the Spray pyrolysis method can be summarized as follows:

(1) Formation of droplets at the nozzle outlet and evaluation of their average size.

(2) Decomposition of the precursor solution on the substrate surface.

a. Starting solution (source)

The composition of the final particle is determined by the dissolved bodies or reagents dissolved in the dissolver (starting solution) in a predetermined stoichiometric ratio. As precursors, usually inexpensive materials such as nitrates, chlorides and acetates are used, which are classified as reagents. Distilled water or alcohol is often used as a solvent. In the basic solution it is necessary to eliminate the problems of solubility and phase segregation, where the different components precipitate at different times. To overcome this and to obtain homogeneous solutions, we recommend adding a small amount of acid (e.g. nitric acid) during the preparation. The overall concentration of the solution can be varied from 0.01 to some moles/liter. Note that this parameter has the effect of changing the average size of the fluid particles ejected. According to the literature, some techniques include preheating of the solution. This preheating can, sometimes, be useful and promotes or accelerates the reaction

on the substrate. This increases the deposition rate and improves the quality of the resulting films [145].

b. Droplet generation (Transport)

The size and homogeneity of the deposited material can be roughly determined from the size of the sprayed droplets and the concentration of the solution while its morphology can also be determined by the concentration and velocity of the droplets produced by the atomizers. Concerning the atomization or the identical way to the production of droplets and their dispersion in the air, several methods of atomization have been used in the studies spray pyrolysis, for example: pneumatic (air is the carrier gas), ultrasonic (pyro sol), gravitation, etc.

In the deposition device, the base solution can be transported to the substrate by the effect of a gas pressure. The gas pressure method has two advantages. Firstly, the flow can be controlled very sensitively and secondly, gases can also be used as secondly, gases can also be used as reactive elements in the composition of the material to be material to be deposited, in this case the semiconductor, such as O_2 for ZnO. However, for most compound semiconductors, N_2 or an inert gas is used to avoid chemical reactions between the compound materials and/or the solvent, which would lead to the addition of addition of impurities. In some cases, in order to prevent the oxidation of the materials, a binary mixture of N_2 and H_2 is used as carrier gas [146].

c. Chemical reaction on the substrate (deposit)

When the aerosol droplets approach the surface of the heated substrate (200-600°C), under appropriate experimental conditions, the vapor formed around the droplet prevents direct contact between the liquid phase and the substrate surface.

This phenomenon occurs above a certain temperature, called the Leidenfrost temperature.

This evaporation of the droplets allows a continuous renewal of the vapor, so the droplets undergo thermal decomposition and give the formation of strongly adherent film.

It is noted that the gas phase decomposition reaction of $ZnCl_2$ occurring on the substrate surface is an endothermic reaction that requires relatively high temperatures for relatively high temperatures for the realization of the decomposition (pyrolysis) of the solutions used (droplets) arriving on heated substrates [145].

II.1.2. Influence of deposition parameters on thin film properties

Thin-film deposition, using the spray pyrolysis technique, involves spraying a metal salt solution onto a heated substrate. Droplets impact on the substrate surface, spread into a disk shaped structure, and undergo thermal decomposition. The shape and size of the disk depends on the momentum and volume of the droplet, as well as the substrate temperature. Consequently, the film is usually composed of overlapping disks of metal salt being converted into oxides on the heated substrate [144].

a.Influence of temperature

Spray pyrolysis involves many processes occurring either simultaneously or sequentially. The most important of these are aerosol generation and transport, solvent evaporation, droplet impact with consecutive spreading, and precursor decomposition. The deposition temperature is involved in all mentioned processes, except in the aerosol generation. Consequently, the substrate surface temperature is the main parameter that determines the film morphology and properties. By increasing the temperature, the film morphology can change from a cracked to a porous microstructure [144].

In many studies the deposition temperature was reported indeed as the most important spray pyrolysis parameter. The properties of deposited films can be varied and thus controlled by changing the deposition temperature, for instance, it influences optical and electrical properties of zinc oxide films [147]. Films with the lowest electrical resistivity were deposited using an aqueous solution of zinc acetate at 490◦C resulting in improved crystallinity, while films prepared at 420 and 490◦C showed high transmission (90–95%) in the visible range. This was attributed to a decrease of the film thickness and an increase in the structural homogeneity [144].

The physical properties of fluorine-doped indium oxide films were investigated with respect to deposition temperature, dopant concentration, air flow rate, and film thickness [148]. It was found that the deposition temperature has a remarkable influence on the structure of the films. The extent of preferential (4 0 0) orientation increases with increasing film thickness. Terbia-doped yttria-stabilized thin films have been deposited using electrostatic spray deposition [149]. The surface morphology was controlled by changing the deposition parameters and solution compositions. By increasing the deposition temperature, the morphology of the film was shifted from a dense to a highly porous structure [144].

b. Influence of precursor solution

The precursor solution is the second important process variable. Solvent, type of salt, concentration of salt, and additives influence the physical and chemical properties of the precursor solution. Therefore, structure and properties of a deposited film can be tailored by changing composition of precursor solution [144].

Chen et al. have shown that the morphology of the thin films can be changed considerably by adding additives to the precursor solutions [150]. The structure of deposited TiO_2 film was changing from a cracked to a crack-free reticular after the introduction of acetic acid into the

precursor solution. The change of morphology was attributed to the modification of precursor solution. Porous SnO_2 and SnO_2-Mn_2O_3 films have been prepared using the electrostatic spray deposition technique [151, 152]. These films were used in Taguchi type hydrogen sensors. The grain size of the porous films ranged from 1 to 10 μm. It was observed that the grain size increases with a higher concentration of the precursor in the ethanol solvent [144].

II.1.3. Choice of spray pyrolysis technique

The spray pyrolysis technique was our choice because of its numerous advantages that make it attractive and competitive compared to many other techniques used for materials synthesis. Examples of these advantages are [153]:

- Spray pyrolysis is cost effective and can be easily performed.

-Substrates with complex geometries can be coated.

- Spray pyrolysis deposition leads to relatively uniform and high quality coatings.

- No high temperatures are required during processing (up to ~ 500 °C).

- Spray pyrolysis does not require high-quality substrates or chemicals.

- Films deposited by spray pyrolysis are reproducible, giving it potential for mass production.

II.1.4. Spray pyrolysis system set-up

Barium-calcium tin oxide and barium lead-tin oxide thin films were deposited onto glass substrates using the spray pyrolysis technique. The experimental set-up of our spray pyrolysis system was carried out at the Laboratory of Research on Physico-Chemistry of Surfaces and Interfaces (LRPCSI) of the University of Skikda. The set-up used is very simple, it is a manual sprayer, in which, we put the deposit solution, the sprayer is fixed at a distance of 20 cm from the substrate, the nozzle of the latter is oriented towards the heated substrate, the

heating plate temperature is displayed by a thermometer from a thermocouple on the substrate.

II.1.5. Preparation of barium-calcium tin oxide and barium lead-tin oxide thin films

In this work, we used the following aqueous solutions as precursor sources:

- 0.01M of barium chloride ($BaCl_2$), source of Ba^{2+}.
- 0.01M of calcium chloride ($CaCl_2$), source of Ca^{2+}.
- 0.01 M of tin chloride ($SnCl_2$), source of Sn^{4+}.
- 0.01 M of lead chloride ($PbCl_2$), source of Pb^{2+}.

For all these precursor solutions, distilled water was used as a solvent. Barium-calcium tin oxide and barium lead-tin oxide thin films were deposited onto glass substrates using the spray pyrolysis technique.

For the barium-calcium tin oxide thin films, the precursor solutions were mixed with volume ratios R_{Ba}:R_{Ca}: R_{Sn} of 0.5:0:0.5, 0.4:0.1:0.5, 0.3:0.2:0.5, 0.2:0.3:0.5, 0.1:0.4:0.5 and 0:0.5:0.5.

For the barium lead-tin oxide thin films, the precursor solutions were mixed with volume ratios R_{Ba}:R_{Pb}: R_{Sn} of 0.5:0:0.5, 0.5:0.1:0.4, 0.5:0.2:0.3, 0.5:0.3:0.2, 0.5:0.4:0.1 and 0.5:0.5:0.

All precursor solutions were sprayed onto the glass substrates kept on a hot metallic plate heated to a temperature of 500 °C. The precursor solutions are manually sprayed using a perfume nozzle.

The distance between the nozzle and the substrate was 20cm. The spray rate was 140 mm^3 per spray and the time between two successive sprays was 1s.

II.2. Characterization Techniques

In this section, the different characterization techniques used to study the effect of the substitution of barium by calcium on structural, optical and luminescence properties of deposited barium tin oxide films are described.

Structural, optical and luminescence characterization of the deposited films is performed by X-ray diffraction (XRD), UV–visible spectroscopy and photoluminescence spectroscopy (PL), respectively. The thickness of the deposited thin films is measured using a profilometer.

II.2.1. X-ray diffraction (XRD)

X-ray diffraction (XRD) is a non–destructive technique used to determine the structural properties of the crystals based on the scattering of light. Since amorphous materials are not organized in a periodic array, they do not scatter light coherently. In a crystal structure each atom is arranged in a periodic array and, when an X-ray interacts with it, a certain amount of energy is absorbed. Electrons occupy certain energy states around an atom, but the absorbed energy is not enough to release the electron, the energy must then be re-emitted in a form of a new x-ray with the same energy as the original, this process is known as elastic scattering. At specific x-ray incident angles, the scattered x-rays can constructively interfere; this is called diffraction and results in a peak in intensity seen in the XRD diffractogram. The diffracted peaks can be associated with different planes in an atom structure and they are named after the (hkl) Miller indices.

In the XRD set-up, the sample under test is exposed to a beam of x-rays with a given incident angle θ as in figure II.2. The diffracted light is received by the X-ray detector in a 2θ angle. Diffraction is used to measure the distance between the atom planes [154].

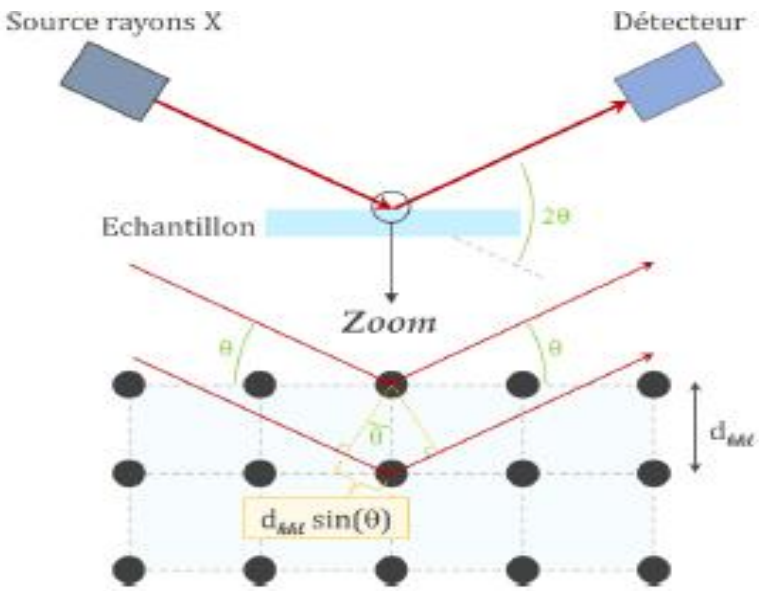

Figure II.2: Schematic representation of the Bragg's equation.

The Bragg's law relates the crystal spacing d_{hkl} with the x-ray wavelength λ and the angle of incidence by the following expression:

$$n\,\lambda = 2\,d\sin\theta \qquad \text{(II.1)}$$

where n is an integer known as the order or reflection. The crystal geometry can be determined from the crystal spacing measured by XRD. XRD technique has been used in this work to determine the crystalline structure of Barium-calcium tin oxide thin films.

a. Lattice parameters

From the crystal spacing, the lattice parameters can be also determined following the expression for a given geometry. For the cubic structure (a = b= c), in which Ba_3SnO and Ca_3SnO perovskite oxides crystallize, the lattice parameter a is given by [155]:

$$a = \frac{0.9\,\lambda}{2\,\sin\theta}\ \sqrt{h^2 + k^2 + l^2} \qquad \text{(II.2)}$$

where *h*, *k*, *l* the Miller indices, λ the x-ray wavelength and θ the angle of diffraction.

b. The crystallites size

The crystallites size of the different samples was determined from the spectra of x-ray diffractions. The crystallites size *D* of thin films was estimated using the Debye-Scherrer's formula given by [155]:

$$D = \frac{0.9\,\lambda}{\beta\,cos\theta} \qquad \text{(II.3)}$$

where λ is the wavelength the x-ray, θ is the diffraction angle and β is the broadening of diffraction line measured at half its maximum intensity of Gaussian fit (in radians).(Figure II.3).

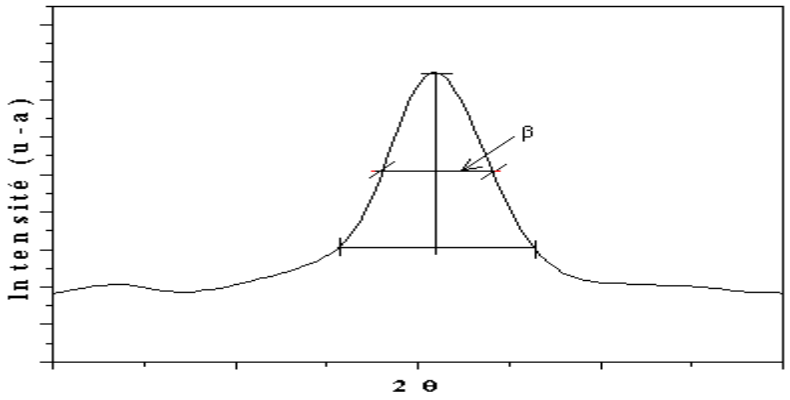

Figure II.3: Illustration showing definition of β from X-ray diffraction peak.

c. Determination of deformations

In general, the deformations are related to the constraints by the formula: $T_{ji} = C_{ijkl} . \sigma_{kl}$. This method requires knowledge of C_{ijkl} elasticity constants. These are sometimes not available in the literature. Another approach to deduce information of deformation in the film, without

using these constants. The latter links the deformation to the broadening of diffraction line measured at half its maximum intensity of Gaussian fit β [156].

$$\varepsilon = \frac{\beta.\cos(\Delta\theta)}{4} \qquad \text{(II.4)}$$

d. Diffractometer

X-ray diffractograms of our samples were obtained using a Rigaku-SmartLab X-ray diffractometer equipped with a monochromatic source delivering a CuKα1 incident beam (9 kW, 0.154056 nm) with an acceleration voltage of 45 mV and a current of 40 mA (Figure II.4).

Figure II.4: Diffractometer used for characterization of the deposited thin films.

The step of the chosen resolution is 0.01, the scan values (θ-2θ) are between 10° and 60°. Each time an angle checks the Bragg law, the counter records an increase in reflected intensity. At the end of the collection of rays diffracted at each angle, a diffraction spectrum is

obtained on which appear characteristic peaks of the structure studied. For the identification of existing phases in the sample, the obtained diffraction spectrum is compared to reference spectra of the expected phases from the JCPDS files.

II.2.2. UV-visible spectroscopy

The Ultraviolet-visible (UV-vis) absorption spectroscopy is a quantitative technique which is used to measure the concentration of absorbing specie in a material, typically, in the range of 200 nm to 800 nm. This is done by measuring the intensity of light that transmitted through a sample with respect to the incident light uv-visible.

The principle of the spectrophotometer is as follow: a source consisting of two lamps that allow a continuum of emission over the entire UV-visible wavelength range. A monochromator allows to select wavelengths and thus to make a sweep of the range by moving this monochromator. The photon beam of selected wavelength passes through a mirror that synchronizes the movement of the monochromator then the beam passes through the sample and the reference. Finally, an amplifier makes it possible to compare the transmitted intensity with the emission intensity [157] (Figure II.5).

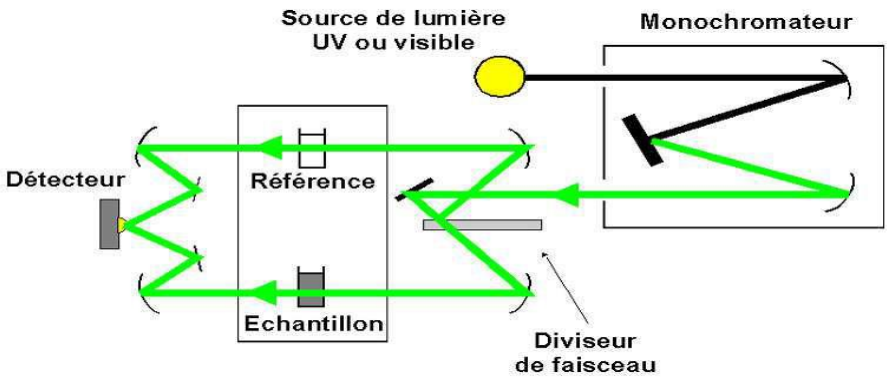

Figure II.5: Schematic representation of UV-visible spectrophotometer [158].

From the UV-Visible spectra it is possible to determine the thickness, the value of the band gap and the optical indices. The transmission and reflection curves were recorded at IPCMS-France using a Perkin Elmer UV-VIS-NIR spectrophotometer of type LAMBDA 950.

The obtained spectrum represents the evolution of the transmission as a function of the wavelength. The transmission T (%) is defined as the ratio of the transmitted light intensity I to the incident light intensity I_0.

a. The absorption coefficient Calculation

We used the Bouguer-Lambert-Beer law to determine the absorption coefficient of the material [159]:

$$T = \exp(-\alpha t) \qquad \text{(II.5)}$$

Equation (II.5) may be written as follows:

$$\alpha\ (cm^{-1}) = \frac{1}{d} \mathrm{Ln}\left(\frac{100}{T\%}\right) \qquad \text{(II.6)}$$

With α: the absorption coefficient, d: film thickness, T: film transmittance.

b. Optical band gap calculation

To estimate the band gap energy Eg in the high absorption range ($\alpha > 10^4 cm^{-1}$), we used Tauc's law [160]:

$$\alpha h\nu = A\,(h\nu - Eg)^{1/2} \qquad \text{(II.7)}$$

where α is the absorption coefficient , d is the film thickness , $h\nu$ is the photon energy, Eg is the optical band gap energy and A is a characteristic parameter independent of photon energy. By plotting $(\alpha h\upsilon)^2$ versus $h\upsilon$ and extrapolating the linear portion of the absorption edge to find

the intercept with energy axis, we can determine the value of the optical gap Eg , as shown in the figure II.6:

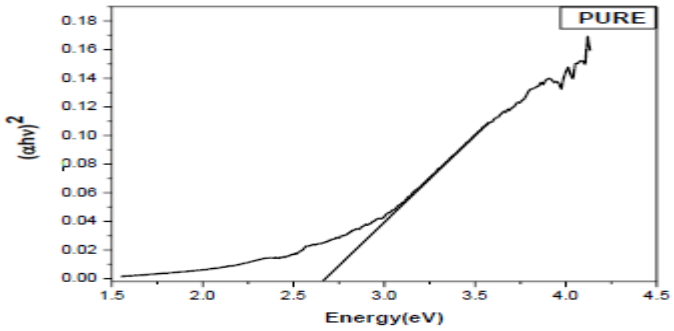

Figure II.6: Determination of the optical gap by extrapolation the linear part of the curve [161].

II.2.3. Photoluminescence spectroscopy.

Photoluminescence is a powerful optical spectroscopy technique for characterizing semiconductor materials and insulators. The principle of photoluminescence (PL) is as follows: a photon of a laser source induced, by optical absorption, the transition of an electron from its ground state, which is a valence state, to an unoccupied conduction state, leaving in its place a hole. The hole and the electron interact with the vibrations of the atomic lattice and emit (or absorb) phonons. Then, the electron and the valence hole recombine radiatively by emitting a photon whose energy differs from that of the exciter phonon.

PL therefore consists of a consecutive light emission following an excitation of energy states by light absorption. The mechanisms that control the PL signal can be classified into three stages (Figure II.7)

1. The creation of excess carriers in the semiconductor by absorption of exciter light (generation of electron-hole pairs and their distribution in the semiconductor).
2. Radiative recombination of excess electrons and holes.

3. The emission of the PL signal from the surface, limited by the reabsorption of photons and internal reflection [162].

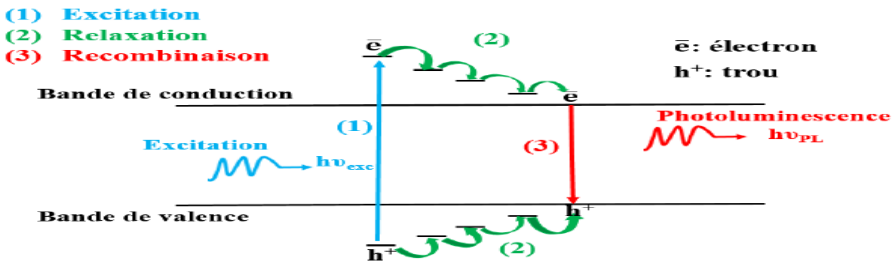

Figure II.7: Formation and recombination of an exciton in a semiconductor [163].

When the electron loses its energy by radiative recombinations and recombines with the hole, the emitted photons make up the photoluminescence spectrum. The different wavelengths composing the PL spectrum reflect the different levels of transition energy allowed in the material (Figure II.8). Therefore, a PL spectrum gives information on the nature of defects present in the material (gaps, interstitial atoms, impurities, …). To calculate the concentration of defects N (in cm^{-3}) from the photoluminescence spectrum, the SMAKULA formula given by [165] is used:

$$N = 1.29 \times 10^{17} \frac{n}{f(n^2+2)^2} \alpha W_{1/2} \qquad \text{(II.8)}$$

where f: the oscillation force related to the probability of the optical transition giving absorption ($f \approx 1$).

n: the refractive index of the crystal at the wavelength considered.

α: the maximum intensity of the emission band.

$W_{1/2}$: the width at mid-height of the emission band expressed in eV.

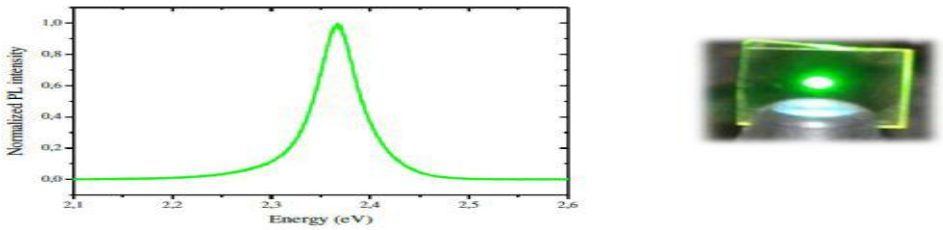

Figure II.8: Photoluminescence of a thin film of PEPI (excitation wavelength is 405 nm, from a laser diode) [164].

In this thesis, the photoluminescence spectra were recorded at room temperature at the IPCMS-France using, as a source of excitation, a 355 nm line of a tripled frequency neodymium-doped yttrium aluminum garnet (Nd-YAG) laser. The PL signal was recorded using a cooled CCD camera with an integration time of 500 ms.

II.2.4. Profilometer

Profilometer is a precise and easy technique for measuring the thickness of thin films. The principle of operation of this apparatus is as follows (Figure II.9). A very sensitive diamond tip stylus scans the surface of the sample, the surface irregularities of the analyzed deposit result directly in a variation in the vertical position of this stylus which is then transformed into electrical voltage through a differential transformer. A digital analytical converter allows storage the results in the device memory and link to the software.

We then obtain on the screen the vertical variation of the position of the stylus according to the distance it has traveled on the sample (the step between the covered substrate area (deposit) and the other uncovered area figure. In our work, the measurement of films thickness was performed using a Dektak 8 profilometer available at the IPCMS-France.

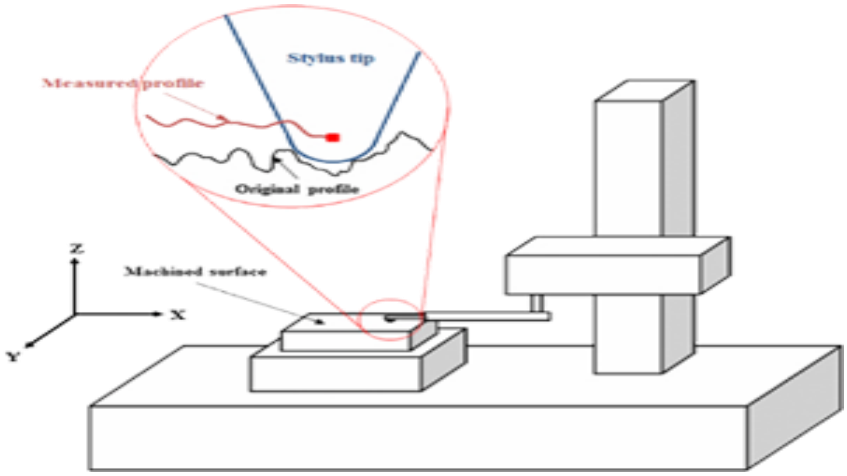

Figure II.9: Schematic of a stylus profilometer.

Chapter III

Results and discussion

This chapter is essentially devoted to the presentation and the discussion of the results of the structural, optical, and photoluminescence characterizations of barium–calcium tin oxide and barium lead-tin oxide thin films, as a function of the calcium-based solution volume ratio R_{Ca} and the lead-based solution volume R_{Pb} respectively. These characterizations were performed by different techniques such as x-ray diffraction (XRD), UV-visible spectrophotometry, photoluminescence (PL) spectroscopy in addition to thickness measurements using the surface profilometry.

III.1. Effect of the substitution of barium by calcium

III.1.1. XRD characterization

It should be noted that structural characterization by x-ray diffraction (XRD) was performed using a Rigaku-SmartLab diffractometer. The X-ray radiation used is the line of copper with a wavelength equal to 1.54056 Å. Figure III.1 shows the x-ray diffractograms of barium-calcium tin oxide thin films deposited by pyrolysis spray as a function of the calcium-based solution volume ratio R_{Ca} from 0 to 0.5.

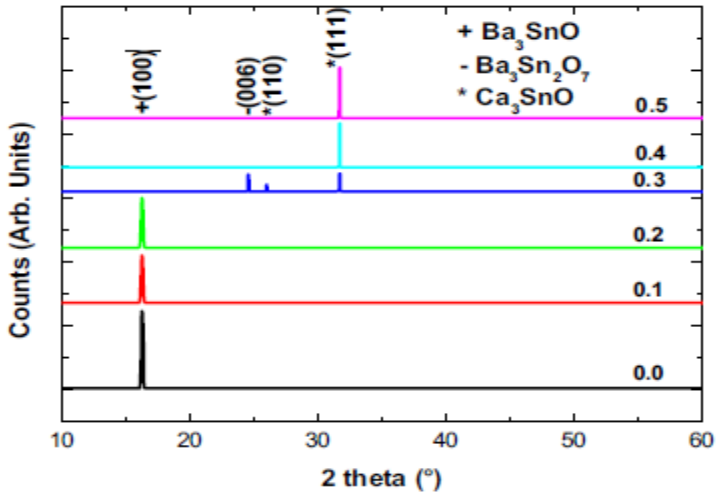

Figure III.1: XRD patterns of barium-calcium tin oxide thin films.

According to the JCPDS# 04-016-3131 record, the diffraction patterns of films with R_{Ca} from 0 to 0.2 are those of the cubic Ba_3SnO phase with one peak located at 16.26° corresponding to the (100) orientation. One can see, for these values of R_{Ca}, that there is no peak corresponding to a calcium-based phase. This indicates that the substitution of barium by calcium, for these R_{Ca} values, did not take effect. The substitution of barium by calcium takes place for R_{Ca} values from 0.3 (Figure III.1) where, for this R_{Ca} value, the two peaks located at 26.43 and 32.06° correspond respectively to the (110) and (111) orientations of the cubic Ca_3SnO phase according to the JCPDS# 00-001-0998 record. For the same volume ratio, i.e. R_{Ca}=0.3, no peak related to the Ba_3SnO phase is observed. The peak located at 24.03° correspond to the (600) orientation of $Ba_3Sn_2O_7$ metastable phase according to the JCPDS# 00-025-0077 record. This shows that the phase transition from Ba_3SnO to Ca_3SnO is not a direct process. Prajapati et al. [166] evidenced the appearing of a secondary phase of $La_3Sn_2O_7$ when doping $BaSnO_3$ with Lanthanum. For R_{Ca} values of 0.4 and 0.5, only the Ca_3SnO phase is present with one peak corresponding to the (111) orientation. The completed phase transition takes place for R_{Ca} value of 0.4.

a. lattice parameter *a*

The variation of the lattice parameter *a* of both phases Ba_3SnO and Ca_3SnO is traced, in figure III.2, as a function of the calcium-based solution volume ratio R_{Ca}. The lattice parameter *a*, for a Ba_3SnO and Ca_3SnO cubic structure thin films, is determined by equation (II.2).

We can see, in figure III.2, that the lattice parameter *a* of the deposited Ba_3SnO films is less than that of the bulk material (a_0=5.448 Å according to the JCPDS# 04-016-3131). This indicates that the deposited thin films were exposed to a compressive stress due to several factors such as the temperature and the difference of the coefficient of thermal dilatation between the substrate and the film. These factors influence also the optical properties of the

deposited films [167]. The slight decrease of the lattice parameter *a* of the Ba_3SnO from 5.461 to 5.452 Å, with the increase of the R_{Ca} from 0 to 0.2, reflects that the effect of the substitution of barium by calcium is not significant despite the atomic radius of calcium (r_{Ca}=197 pm) is less than that of the barium (r_{Ba}=217 pm). However, the fact that the lattice parameter of the bulk Ba_3SnO is greater than that of the bulk Ca_3SnO (a_0=4.834 Å according to the JCPDS# 001-0998) suggests that the compressive stress in the Ba_3SnO films could be also related to the phase transition from Ba_3SnO to Ca_3SnO induced by the substitution of barium by calcium. For R_{Ca} values from 0.3 to 0.5, the decrease of the lattice parameter *a* of the Ca_3SnO phase from 4.882 Å to 4.846 Å reflects a stress relaxation. The stabilization of the lattice parameter a, corresponding to calcium-based solution volume ratios of 0.4 and 0.5, at values close to the lattice parameter of the bulk Ca_3SnO is related to the presence of this only phase which is not the case for the lattice parameter of the sample corresponding to R_{Ca}=0.3. The high value of the lattice parameter corresponding to R_{Ca}=0.3 may be related to the presence of the $Ba_3Sn_2O_7$ phase which could be the cause of the stretching stress.

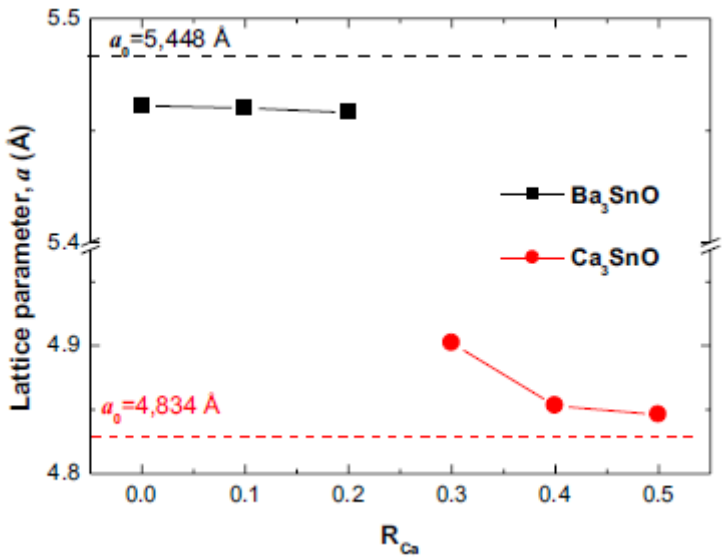

Figure III.2: Variation of the lattice parameter a as a function of calcium-based solution volume ratio R_{Ca}.

b. Crystallites size D

The crystallites size *D* of Ba_3SnO and Ca_3SnO thin films was determined using equation (III.3). Figure III.3 shows The Ba_3SnO and the Ca_3SnO crystallites size *D* and their corresponding peaks intensity as a function of the calcium-based solution volume ratio R_{Ca}.

As can be seen in figure III.3, the different crystallites size, as well as, their corresponding peaks intensity varies as a function of R_{Ca}. In figure III.3.a, the (100)-oriented Ba_3SnO crystallite size remains invariant, around 37 nm, when R_{Ca} is between 0.0 and 0.2. Given the correlation between the XRD peak intensity and the number of its corresponding crystallites, the (100)-oriented Ba_3SnO crystallites number start decreasing from R_{Ca}=0.1 (Figure III.3.b) which indicates that for these volume ratios, even the Ca_3SnO is not formed, the substitution of barium by calcium induced the destruction of the cubic Ba_3SnO crystallites and may be a formation of some amorphous calcium-based phases. Gholizadeh [168] evidenced the phase structure transition when substituting Fe by Co and La by Sr in lanthanum ferrite nanoparticles. For R_{Ca}=0.3, where the Ba_3SnO phase completely disappears, the Ca_3SnO phase appears with (110) and (111)-oriented crystallites size of 36 and 45 nm respectively (Figure III.3.a). The number of (110) and (111)-oriented crystallites is less than that of the (100)-oriented Ba_3SnO crystallites for R_{Ca} values from 0 to 0.2 (Figure III.3.b). Despite the size of the (006)-oriented $Ba_3Sn_2O_7$ metastable phase crystallites (60 nm), is greater than that of both (110) and (111)-oriented Ca_3SnO crystallites (Figure III.3.a), their number remains comparable (Figure III.3.b). This could be explained by the fact that the formation of the Ca_3SnO crystallites, due to the presence of a considerable quantity of the calcium cations, exerted internal stress on the (100)-oriented Ba_3SnO crystallites inducing their phase transition to (006)-oriented $Ba_3Sn_2O_7$ crystallites.

The stress induced phase transition of was theoretically and experimentally evidenced on several materials [169-172]. For R_{Ca} values of 0.4 and 0.5, the crystallite size of the (111)-

oriented Ca_3SnO phase, which remains constant around 95 nm, is approximately two and a half times greater than that of the (100)-oriented Ba_3SnO crystallites when R_{Ca} is between 0 and 0.2 (Figure III.3.a) while their number is approximately one and a half time less than that of the (100)-oriented Ba_3SnO crystallites. This could be explained by the fact that two different materials, such as Ba_3SnO and Ca_3SnO, could not have the characteristics when elaborating using the same experimental conditions.

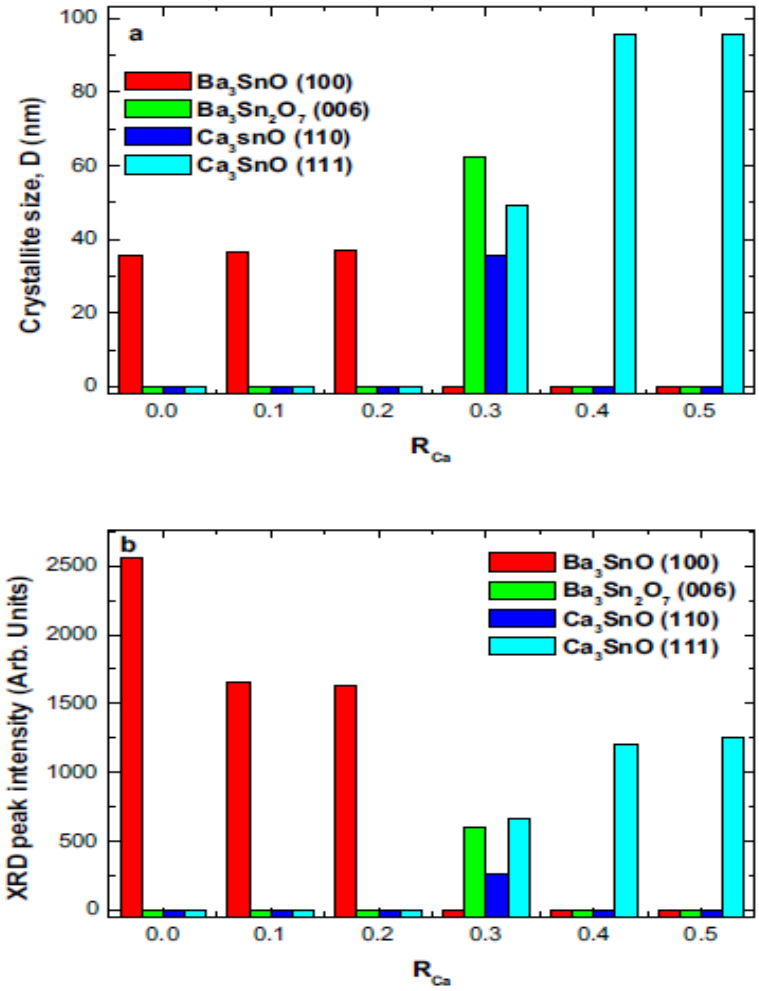

Figure III.3: Variation of: **a)** the crystallites size and **b)** the corresponding peaks intensity as a function of calcium-based solution volume ratio R_{Ca}.

III.1.2. UV-visible characterization

Figure III.4 presents the variation of transmittance spectra, in the UV-visible domain, as a function of the calcium-based solution volume ratio R_{Ca}. As can be seen, the shape of transmittance spectra is invariant, as a function of R_{Ca}, except for R_{Ca}=0, i.e. for the Ba_3SnO phase, which exhibit a different shape. This shows that the weak presence of calcium in the Ba_3SnO matrix for R_{Ca}=0.1 and 0.2, which has no effect on the crystalline phase transition (Figure III.1), increases significantly the optical transmittance of the deposited films. As a function of the calcium-based solution volume ratio R_{Ca}, the mean transmittance, calculated in the visible spectral domain (Figure III.5), increases from 50% for R_{Ca}=0, which correspond to the Ba_3SnO phase, to reach 80% for R_{Ca}=0.5, which correspond to the Ca_3SnO phase. Many works have been done on the effect of calcium on the optical transmittance of materials. Zhu et al. [173] reported the increase of scintillation ceramics transmittance after doping with calcium. The role of calcium in increasing the optical transmittance was also evidenced by Yücel et al. [174] when doping PbS with calcium.

a. The film thickness d

The measurement of barium-calcium films thickness was performed using a Dektak 8 profilometer. The films thickness *d* is also traced, in figure III.5, as a function of R_{Ca}. As can be seen, the films thickness *d* decreases, as a function of R_{Ca} from 120 to 85 nm and it correlates with the increase of the optical transmittance which is in good agreement with results in [175, 176]. In this work, the decrease of the thickness could be related to the crystallographic parameters such as lattice parameters and crystallites size which depend directly on the experimental conditions of films deposition. However, establishing a direct relation between the thickness and these parameters is not evident due to the presence of other

factors that directly influence the films thickness such as surface roughness [177] and porosity [178].

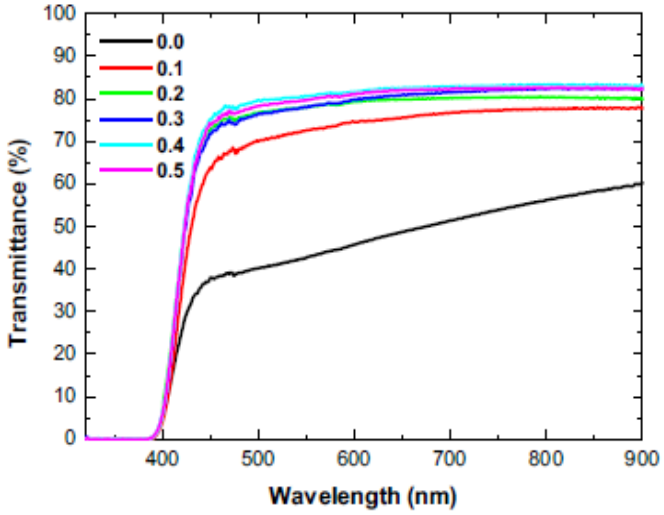

Figure III.4: Optical transmittance spectra of barium-calcium tin oxide films deposited with calcium-based solution volume ratio R_{Ca} from 0 to 0.5.

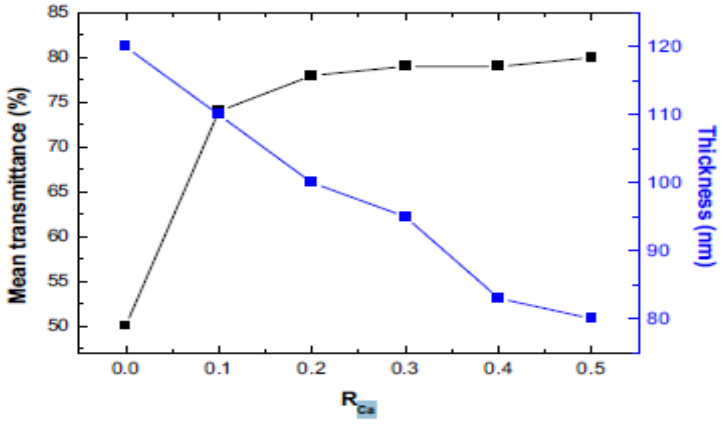

Figure III.5: Variation of the mean transmittance and the films thickness as a function of calcium-based solution volume ratio R_{Ca}.

b. Optical band gap energy

The optical band gap energy of barium-calcium thin films was estimated using the equation (II.7) by extrapolation of the linear part of $(\alpha h\nu)^2$ to $h\nu=0$ (Figure III.6). The variation of the band gap energy as a function of R_{Ca} is shown in the inset of figure III.6.

As can be seen, the band gap energy decreases from 3.14 eV, for R_{Ca}=0.0 which correspond to the Ba_3SnO phase, to 3.09 eV, for R_{Ca}=0.5 which correspond to the Ca_3SnO phase. The effect of the calcium addition on the decrease of the band gap energy was evidenced before by Omran et al. [179] when doped PZT with calcium. The decrease of the band gap energy by doping was also observed in organic materials such as PMMA when doping with CeO_2/SiO_2 [180] and Si_3N_4/PEG [173], polycarbonate when doping with SiC/T_aC [174] and polystyrene when doping with $SiO_2/SrTiO_3$ [181]. The band gap values correlate with that in [182] and show that all the deposited films have a semiconducting behavior that allows them to be used in many domains such as gas sensing [183] and solar cells [184].

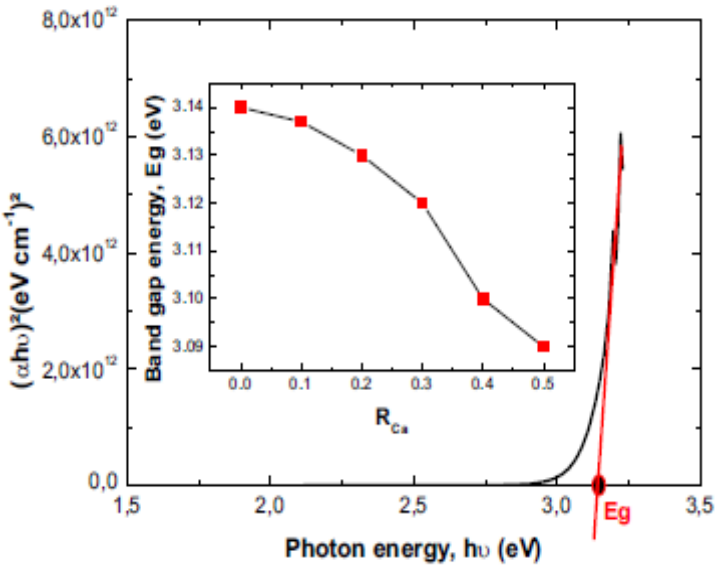

Figure III.6: Plot of (Alpha E) ² as a function of the energy E (Inset: Variation of the band gap energy as a function of calcium-based solution volume ratio R_{Ca}).

III.1.3. Photoluminescence spectroscopy characterization

The photoluminescence spectra (PL) of barium-calcium thin films recorded at room temperature using a source of excitation of 355 nm are presented in figure III.7 as a function of the calcium-based solution volume ratio R_{Ca}. We can see that the substitution of barium by calcium does not affect the main shape of PL spectra however, it increases the PL emission as soon as the calcium is added i.e. from R_{Ca}=0.1. The role of calcium addition in increasing the PL emission was evidenced in phosphors by Fang et al. [185]. The colors emission is originated from the presence of point defects such as oxygen vacancies, metal interstitials, metal vacancies and clusters [186]. We focus on oxygen vacancies because of the important role that they play in the electrical conductivity of metal oxide materials [187]. The emission in the violet region is due to the presence of neutral oxygen vacancies (V_O) [188]. The blue emission is due to the presence of mono ionized oxygen vacancies (V_O^+) while the green emission is due to the presence of double ionized oxygen vacancies (V_O^{++}) [189, 190]. To determine the effect of calcium on the contribution of oxygen vacancies in the violet, the blue and the green emissions, each PL spectrum is deconvoluted into Gaussian peaks.

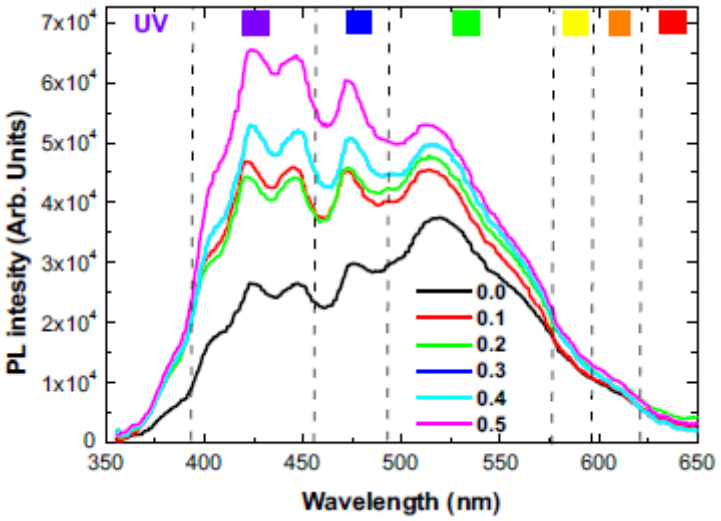

Figure III.7: PL spectra of barium calcium tin oxide films deposited with calcium-based solution volume ratio R_{Ca} from 0 to 0.5.

An example of a PL spectrum deconvolution is presented in figure III.8. In addition to the emission peaks of oxygen vacancies (Figure III.8), three peaks at 384, 561 and 595 nm could be attributed to other types of defects. Their areas are insignificant in front of those of oxygen vacancies corresponding peaks which indicate that the emission is mainly due the presence of the three types of oxygen vacancies. According to Smakula's formula [165], the point defect concentration is proportional to the defect corresponding peak area.

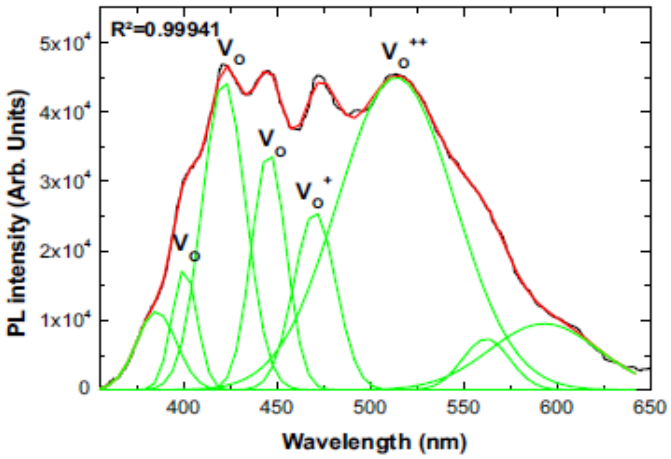

Figure III.8: Example of a deconvolution of a PL spectrum.

The variation of oxygen vacancies corresponding peaks area is plotted, as a function of R_{Ca}, in figure III.9. We can see that the green emission is greater than that of both the violet and the blue emissions. This indicates that the substitution of barium by calcium in Ba_3SnO increases the generation of double ionized oxygen vacancies (V_O^{++}). The same observation could be done for the generation of neutral oxygen vacancies (V_O). The blue emission remains invariant as a function of R_{Ca} which reveals that the substitution of barium by calcium does not affect the mono ionized oxygen vacancies (V_O^{+}). The substitution of barium by calcium induced an increase of V_O^{++} donor defect which makes this material very promising in gas sensing and solar cells domains.

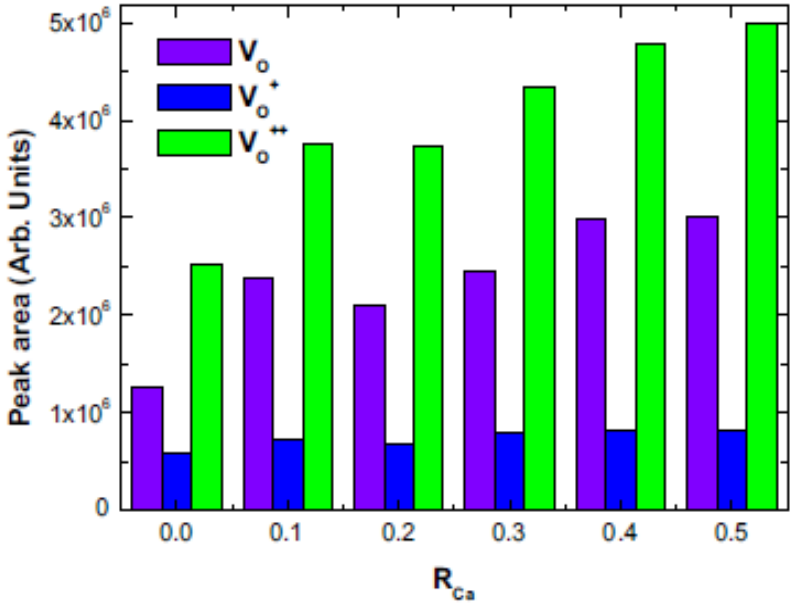

Figure III.9: Variation of oxygen vacancies corresponding emission peaks areas as a function of calcium-based solution volume ratio R_{Ca}.

III.2. Effect of the substitution of tin by lead

III.2.1. XRD characterization

Figure III.10 presents XRD patterns of barium tin oxide films as a function of the lead-based solution volume ratio $R_{Pb.}$ As can be seen in this figure, the phase of the deposited films changes from cubic structure Ba_3SnO to cubic structure Ba_3PbO as a function of R_{Pb}. We can also see that this phase transition is an indirect process. For R_{Pb} equal 0.0 and 0.1, no effect of the substitution of tin by lead can be observed. Only the (100)-oriented Ba_3SnO phase is obtained according to the JCPDS# 04-016-3131 record. For lead-based volume ratio of 0.2, a multiphase structure is obtained composed of, in addition to Ba_3SnO phase, Ba_2PbO_4 phase, according to the JCPDS#12-0666 record, and $Ba_{1.2}Pb_{2.8}O_4$ according to the JCPDS#47-0877 record.

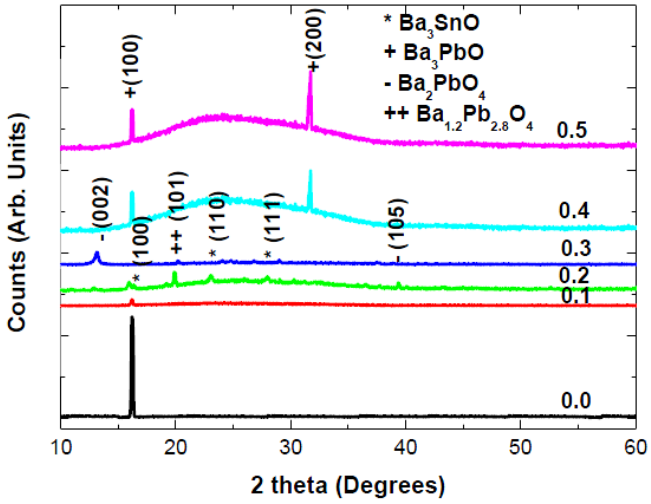

Figure III.10: XRD patterns of barium lead-tin oxide films.

For R_{Pb}=0.2, the Ba_3SnO phase is present in these films by grains oriented (110) and (111), the $Ba_{1.2}Pb_{2.8}O4$ phase is present by grains oriented (101) and the Ba_2PbO_4 phase is present by grains oriented (105). These phases disappeared slightly leading the place to (002)-oriented grains of Ba_2PbO_4 phase for the lead-based volume ratio of 0.3. When R_{Pb}=0.4 and 0.5, on can see that only the Ba_3PbO phase is present in the deposited films with two peaks corresponding to (100) and (200) plans according to the JCPDS#00-001-0998 record. This indicates that from a lead-based solution volume ratio of 0.4, Pb atoms substitutes all Sn atoms in the Ba_3SnO matrix which involve the formation of Ba_3PbO.

a. Lattice parameter

The variation of the lattice parameter of both Ba_3SnO and Ba_3PbO crystals is traced, in figure III.11, as a function to the lead-based solution volume ratio R_{Pb}. We can see that the lattice parameter of Ba_3SnO increases as a function of the lead-based solution volume ratio which reflects the effect of the substitution of tin by lead in the studied samples despite the absence

of the lead related phases peaks in the XRD patterns (Figure III.10). The increase of the lattice parameter for the Ba_3SnO surpassed the reference value (a_0=5.448 Å according to the JCPDS# 04-016-3131) which reflects the presence of stretching stress. This type of stress is also exerted on the elaborated samples using a lead-based solution volume of 0.4 and 0.5 i.e. for the Ba_3PbO phase. For this phase the lattice parameter is invariant as a function of the lead-based solution volume ratio however, it is greater than that of the bulk material (a_0=5.449 Å according to the JCPDS# 00-001-0998).

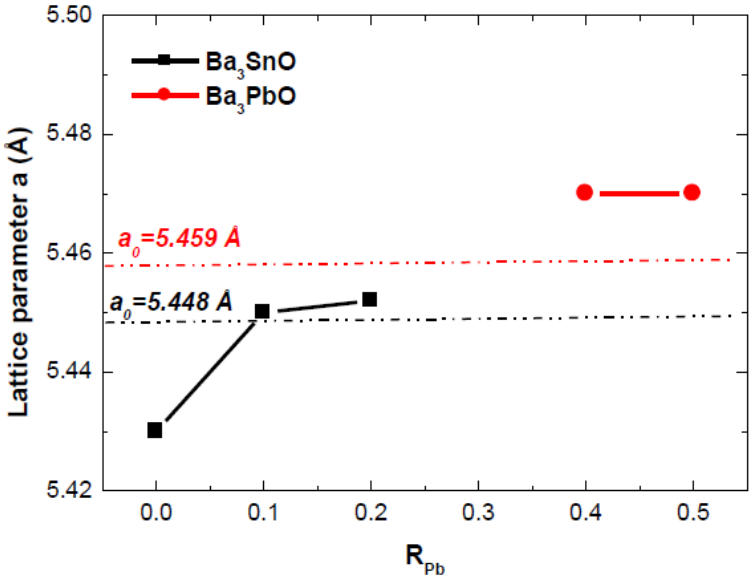

Figure III.11: Variation of the lattice parameter of Ba_3SnO and Ba_3PbO as a function of lead-based solution volume ratio R_{Pb}.

b. Crystallites size

In figure III.12 is presented the variation of the crystallite size *D*, as a function of lead-based solution volume ratio R_{Pb}. One can see that the crystallite size varied from a phase to another as a function of R_{Pb}. The increase of the crystallite size, for R_{Pb} = 0.0 and R_{Pb}=0.1 (Figure

III.12-a), is accompanied by a rapid decrease of the corresponding crystallite number (Figure III.12-b) when supposing the correlation between this parameter and the XRD peak intensity. This may be interpreted by a destruction of the Ba_3SnO (100) crystallites caused by the presence of lead in the material matrix.

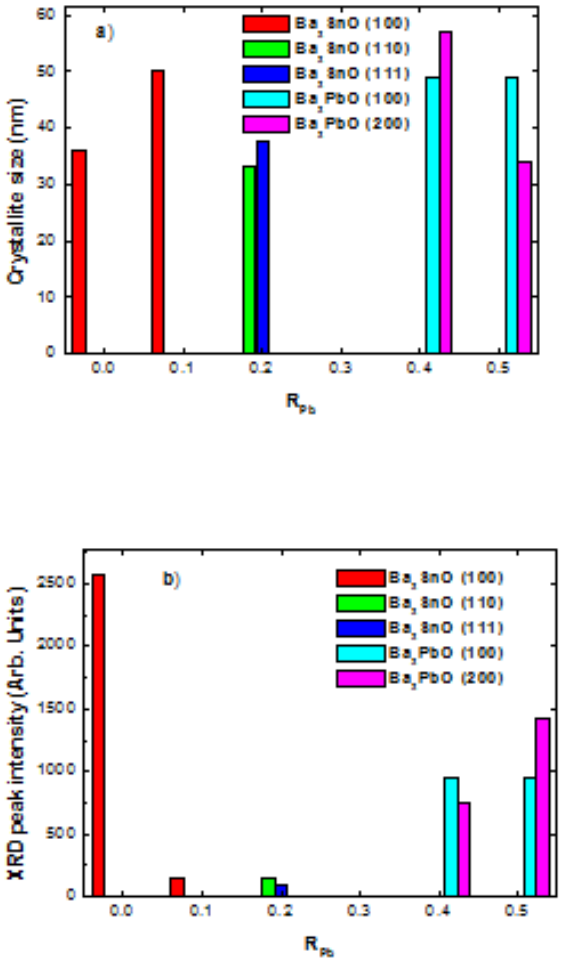

Figure III.12: Variation, as a function of the lead-based solution volume ratio, of: a) the crystallite size and b) the XRD peaks intensity.

This suggestion could be enforced by the disappearing of (100)-oriented crystallites of the Ba_3SnO phase for R_{Pb}=0.2. For this lead-based solution volume ratio, this disappearing of

these crystallites coincides with the appearing of crystallites oriented (110) and (111) which indicate that the exerted stress caused by the substitution of tin by lead atoms may induce the rotation of (100)-oriented crystallites. According to figure III.12-b, the number of the (110) and the (111)-oriented crystallites in the Ba_3SnO phase is less than that of the (100)-oriented crystallites. For R_{Pb}=0.4 and R_{Pb}=0.5 where the only obtained phase is Ba_3PbO, we can see that the (100) oriented crystallites are invariant while for the (200) oriented crystallites, the decrease of their size is accompanied with the increase of their number which may indicate a stress relaxation without change of the crystals orientation.

III.2.3. Photoluminescence spectroscopy characterization

The photoluminescence spectra of the barium lead-tin oxide films are presented, in figure III.13 as a function of the lead-based solution volume ratio R_{Pb}. We can see that the shape of spectra remains invariant which indicates no modification of the nature of defects can be induced by the substitution of tin atoms by lead atoms.

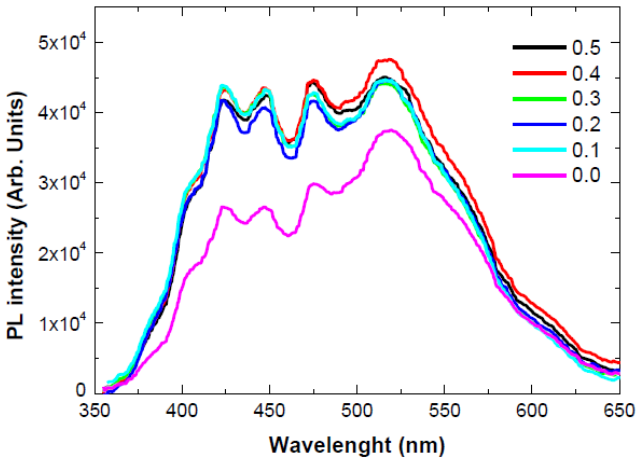

Figure III.13: PL spectra of barium lead-tin oxide thin films.

The effect of the presence of Pb atoms in the Ba_3SnO matrix is evident since it influences directly the PL emission intensity as we can see in figure III.13. We can see also that the PL emission intensity is slightly invariant for the lead-based solution volume ratio from 0.1 which indicates that the substitution of tin atoms by lead atoms does not affect the concentration of the defects present in the deposited films.

The variation of V_O, V_O^+ and V_O^{++} defects related peaks areas is presented, in figure III.14, as a function of lead-based solution volume ratio R_{Pb}. We remain that values were obtained from a PL spectrum deconvolution as showed in figure III.8. As cans be seen in figure III.14, no modification of the three types of oxygen defect concentration when R_{Pb} =0.1. After this value, one can see that the substitution of tin by lead does not really affect the oxygen defects concentration. For all samples, the dominant donor defect is the double ionized oxygen vacancies which play a major role in enhancing the electrical conductivity and this make samples suited for application in PV devices.

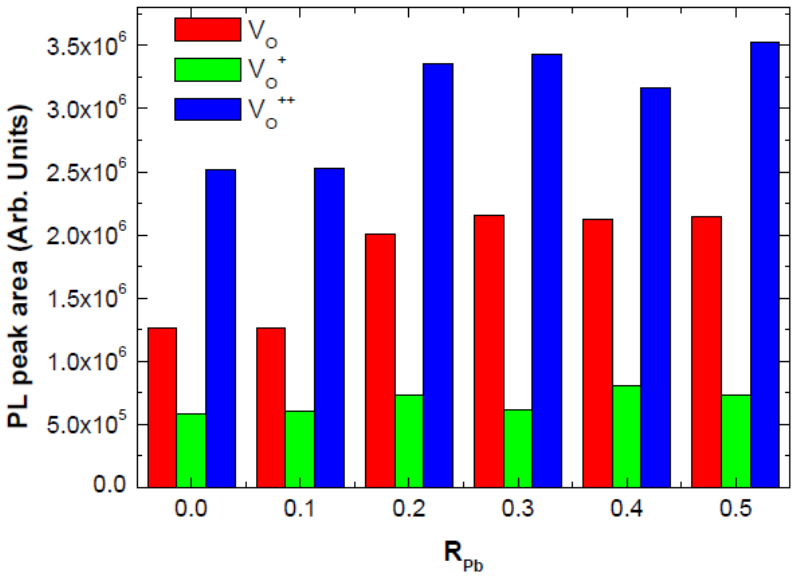

Figure III.14: Variation of oxygen vacancies related peaks area as a function of $R_{Pb.}$

General conclusion

General conclusion

In this work, we studied the effect of the substitution of barium by calcium and tin by lead on physical properties of barium tin oxide thin films deposited onto glass substrates using the spray pyrolysis technique. The effect of substitution on the physical properties is studied as function of respectively, the calcium-based solution volume ratio R_{Ca} and the lead-based solution volume ratio R_{Pb}. All experiments were done at a substrate temperature of 500°C, optimum temperature selected and determined by previous studies. The structural, optical and luminescence properties of the deposited films are investigated by means of x-ray diffraction (XRD), UV-visible spectroscopy and photoluminescence (PL), respectively.

According to the XRD patterns, the substitution of barium by calcium induced an indirect phase transition from Ba_3SnO to Ca_3SnO. The $Ba_3Sn_2O_7$ metastable phase was identified for R_{Ca}=0.3. The variation, as a function of R_{Ca}, of the lattice parameter, crystallites size and XRD peaks intensity exhibited the effect of barium substitution by calcium on the structural properties of the deposited films. The UV-visible spectroscopy evidenced the effect of the substitution of barium by calcium on the enhancement of the optical transmittance. The mean transmittance, in the visible region, increased from 50% for Ba_3SnO (R_{Ca}=0) to 80% for Ca_3SnO (R_{Ca}=0.5) while the films thickness decreased from 120 to 85 nm. The band gap energy of the deposited films decreased slightly from 3.14 to 3.09 eV as a function of R_{Ca}. The semiconducting behavior of the deposited films made them suitable for gas sensing and solar cells. PL spectroscopy showed that the substitution of barium by calcium induces a decrease of the blue emission, which is due to the presence of mono ionized oxygen vacancies (V_O^+) and an increase of the green and the violet emissions, which are due to the presence of double ionized oxygen vacancies (V_O^{++}) and neutral oxygen vacancies (V_O) respectively. The presence of such donor defects made of Ba_3SnO and Ca_3SnO promising materials for optoelectronic and photovoltaic devices.

The XRD patterns of barium lead-tin oxide films showed that the phase transition from Ba3SnO to Ba_3PbO is indirect as a function of the lead-based solution volume ratio. Other phases like Ba_2PbO_4 and $Ba_{1.2}Pb_{2.8}O_4$ were present for R_{Pb}=0.2 and R_{Pb}=0.3. The variation of the crystallite size and the crystallite number suggested that the substitution of tin atoms by lead atoms caused directly the destruction of (100)-oriented crystallites in Ba_3SnO phase by inducing stretching and rotative stress. PL spectra of the deposited films showed the direct effect of the presence of Pb atoms in Ba_3SnO matrix which consists on the increase of the PL emission intensity and then the increase of the present defects such as V_O, V_O^+ and V_O^{++}. The structural and optical characteristics of the deposited Ba_3SnO, Ca_3SnO and Ba_3PbO thin films suggested that they could be used efficiently in photovoltaic applications.

Bibliography

Bibliography

[1] G. Thomas, Nature 389, 907 (1997).

[2] K. Hayashi, S. Matsuishi, T. Kamiya, M. Hirano, and H. Hosono, Nature 419, 462 (2002).

[3] L. Geske, V. Lorenz, T. Muller, L. Jager, H. Beige, H. P. Abicht, and V. Mueller, J. Eur. Ceram. Soc. 25, 2537 (2005).

[4] U. Lampe, J. Gerblinger, and H. Meixner, Sens. Actuators, B 26, 97 (1995).

[5] U. Lampe, J. Gerblinger, and H. Meixner, Sens. Actuators, B 18, 132 (1994).

[6] S. V. Manorama, C. V. G. Reddy, and V. J. Rao, Appl. Surf. Sci. 174, 93 (2001).

[7] M. Bilal, S. Jalali-Asadabadi, R. Ahmad, & I. Ahmad, Journal of Chemistry, 2015, 495131 (2015).

[8] T. Kariyado, and M. Ogata, J. Phys. Soc. Jpn. 80, 083704 (2011).

[9] M. Klintenberg, J. T. Haraldsen, and A. V. Balatsky, Appl. Phys. Res. 6, 31 (2014).

[10] T. H. Hsieh, J. Liu, and L. Fu, Phys. Rev. B 90, 081112 (2014).

[11] M. Oudah, A. Ikeda, J. N. Hausmann, S. Yonezawa, T. Fukumoto, S. Kobayashi, M. Sato, and Y. Maeno, Nat. Commun. **7**, 13617 (2016).

[12] Y. Okamoto, A. Sakamaki, and K. Takenaka, J. Appl. Phys. 119, 205106 (2016).

[13] K. Haddadi, A. Bouhemadou, L. Louail, S. Bin-Omran Solid State Communications 150, 1995 (2010).

[14] C. Röhr, Z. Kristallogr. 210, 781 (1995).

[15] A. Widera, H. Schäfer, J. Less-Common Met. 77, 29 (1981).

[16] S. Yahiaoui, Magister Thesis, Biskra University, Algeria, (2014).

[17] D. Royer and E. Dieulesaint, "Ondes élastiques dans les solides (Génération, interaction acousto-optique, applications)", Edition Masson, Tome 2, France (1999).

[18] Z. Fares, Doctorate Thesis (2021).

[19] M. Boussafeur, Master thesis, Larbi Ben M Hidi University Oum El-Bouaghi, Algeria, (2012).

[20] J. Aronovich, A. Ortiz and R. H. Bube, J.Vac.Sci. Technol. 16.994 (1979).

[21] J. F. Chang, C. C. Shen and M. H. Hon, Ceramics Internet 29 (2003).

[22] https://www.cefi.org (Fra DESS.old / dess_265 html).

[23] G.B. Williamson, R.C. Smallman, Philos. Mag. 1, 15 (1956).

[24] S. Yamaga, A. Yoshokawa, H. Kasain, Cryst. Growth 86 (1998).

[25] I.C. Ndukwe, Sol. Energy Mater. Ground, Cells 40 (1996).

[26] T. E. Varitimos, R.W. Tustison, thin Solid Films 151 (1987).

[27] W.A. Bryant, *J. Mater. Sci*., **12**(7), 1285 (1977).

[28] R.N. Ghoshtagore, *J. Electrochem. Soc.*, **125**(1), 110 (1978).

[29] T. Suntola, *Thin Solid Films*, **216**(1), 84 (1992).

[30] R.R. Chamberlin and J.S. Skarman, *J. Electrochem. Soc.*, 113(1), 86 (1966).

[31] C.J. Brinker, A.J. Hurd, G.C. Frye, K.J. Ward, and C.S. Ashley, *J. Non-Cryst. Solids*, **121**(1–3), 294 (1990).

[32] C.C. Chen, M.M. Nasrallah, and H.U. Anderson, J. Electrochem. Soc., 140(12), 3555 (1993).

[33] C.J. Brinker, G.C. Frye, A.J. Hurd, and C.S. Ashley, Thin Solid Films, 201(1), 97 (1991).

[34] S. Rahmane, Doctorate thesis, Université Mohamed Kheider– Biskra, Algérie, (2008).

[35] https://www.researchgate.net/figure/10-Cathodic-sputtering-accelerated-Ar-ionsextract atoms-from-the-target_fig9_278637056 [accessed 16 May, 2020].

[36] H. Khachab, Doctorate Thesis, Université Abou-Bekr Belkaid -Tlemcen, Algérie, (2010).

[37] G. Tourbot, Doctorate Thesis, Université de Grenoble, France, (2012).

[38] A. Taabouche, Doctorate Thesis, Université Frères Mentouri Constantine I, Algérie, (2015).

[39] K. C. Sanal, PhD Thesis, Cochin University of science and technology, (2014).

[40] K. Badeker, Annalen der Physik 327, 749-66.

[41] C. M. Wang, C.Y. Wen, Y.C. Chen, K.S. Kao, D.L. Cheng, C.H. Peng, Integrated Ferroelectrics, 158, 62-28 (2014).

[42] E. Martinez-Guerrero, Doctorate Thesis, Institut National des Sciences Appliquées de Lyon, France, (2002).

[43] M. Magdalena Şovar, Doctorate Thesis, INP Toulouse et Université Polytechnique de Bucarest, Romania (2006).

[44] B. Romain, Doctorate Thesis, Limoges, (2006).

[45] A. Gaudone, Doctorate Thesis, Limoges, (2005).

[46] J. Livage, Sol-gel synthesis of solids, Encyclopedia of Inorganic Chemistry, R. Bruce King and. John Wiley edition, New York, 3836-3851, (1994).

[47] https://str.llnl.gov/str/May05/Satcher.html, Novel Materials from Sol-gel Chemistry, Lawrence Livermore National Laboratory, 2005.

[48] L. Holland, Vacuum deposition of thin films. First Edition, Published 1956 by Wiley & Sons.

[49] H. Y. Hwang, Y. Iwasa, M. Kawasaki, B. Keimer, N. Nagaosa, and Y. Tokura, Nat. Mater. 11, 103 (2012)

[50] M. Oudah, A. Ikeda, J.N. Hausmann, S. Yonezawa, T. Fukumoto, S. Kobayashi, M. Sato, Y. Maeno, Nat. Commun. 7, 13617 (2016).

[51] A. Hashim, B Mohammed, A.Hadi, H. Ibrahim, J Inorg Organomet Polym, 2023.

[52] M. Bilal, S. J. Asadabadi, R. Ahmad, I. Ahmad, J. Chem. 2015, 495131 (2015).

[53] Y. H. O. Muñoz, M. Ponce, J. E. R. Páez, Powder Tech. 279, 86 (2015).

[54] W. Lu, S. Jiang, D. Zhou, S. Gong, Sens. Actuators B, 80, 35 (2000).

[55] J. Cerdà, J. Arbiol, G. Dezanneau, R. Díaz, J. R. Morante, Sens. Actuators.

[56] K. Ganguly, Doctorate Thesis, University of Minnesota (2018).

[57] P.P. Khirade, A.V. Raut, Perovskite Structured Materials: Synthesis, Structure, Physical Properties and Applications. In Recent Advances in Multifunctional Perovskite Materials. IntechOpen (2022).

[58] M. Johnsson and P. Lemmens, J. Phys. 20, 264001 (2008).

[59] J. M. Rondinelli, S. J. May, and J. W. Freeland, MRS Bull. **37**, 261 (2012).

[60] M.A. Boubchir, Doctorate Thesis, (2022).

[61] A. Prakash, Doctorate Thesis, University of Minnesota (2019).

[62] T. Higuchi, et al. Phys. Rev. B 57, 6978 (1998).

[63] J. Son et al. Nat. Mater. 9, 482, 152 (2010).

[64] J. M. Edge, Y. Kedem, U. Aschauer, N. A. Spaldin, A. V. Balatsky, Phys. Rev. Lett. 115, 247002 (2015).

[65] K. Dunnett, A. Narayan, N. A. Spaldin, A. V. Balatsky, Phys. Rev. B 97, 144506 (2018).

[66] H. J. Kim, U. Kim, T. H. Kim, J. Kim, H. M. Kim, B. G. Jeon, W. J. Lee, H. S. Mun, K. T. Hong, J. Yu, K. Char, and K. H. Kim, Phys. Rev. B **86**, 165205 (2012).

[67] X. Luo, Y. S. Oh, A. Sirenko, P. Gao, T. A. Tyson, K. Char, and S. W. Cheong, Appl. Phys. Lett. **100**, 172112 (2012).

[68] W. Wu, Doctorate Thesis, University of California, Santa Barbara (2023).

[69] A. Kojima, K. Teshima, Y. Shirai, T. Miyasaka, *J. Am. Chem. Soc.* **131**, 6050-6051 (2009).

[70] M. Liu, M. B. Johnston, H. J. Snaith, *Nature* **501**, 395-398 (2013).

[71] R.C. Ropp, Encyclopedia of the alkaline earth compounds. Newnes (2012).

[72] J.-M. Herrmann, M.R. Nunes, F.M. da Costa, Journal of the Chemical Society, Faraday Transactions 1: Physical Chemistry in Condensed Phases, 78, 1983-1991 (1982).

[73] G. Larramona, C. Gutiérrez, I. Pereira, M.R. Nunes, F.M.A. da Costa, Journal of the Chemical Society, Faraday Transactions 1: Physical Chemistry in Condensed Phases, 85, 907-916 (1989).

[74] R. Cava, B. Batlogg, R. van Dover, P. Gammel, J. Krajewski, W. Peck Jr, L. Rupp Jr, in: AIP Conference Proceedings, American Institute of Physics, 55-64 (1991).

[75] D. Singh, D. Papaconstantopoulos, J. Julien, F. Cyrot-Lackmann, Physical Review B, 44, 9519 (1991).

[76] R. Claessen, M.G. Smith, J.B. Goodenough, J.W. Allen, Physical Review B, 47, 1788-1793 (1993).

[77] H. Yun, M. Topsakal, A. Prakash, K. Ganguly, C. Leighton, B. Jalan, R. M. Wentzcovitch, K. A. Mkhoyan, and J. S. Jeong, J. Vac. Sci. Technol. A 36, 031503 (2018).

[78] Y. Li, L. Zhang, Y. Ma, and D. J. Singh, APL Mater. 3, 011102 (2015).

[79] D. J. Singh, Q. Xu, and K. P. Ong, Appl. Phys. Lett. 104, 011910 (2014).

[80] Qinzhuang Liu, Jianming Dai, Zhongliang Liu, Xiaobo Zhang, Guangping Zhu, and Guohua Ding, J. Phys. D: Appl. Phys. 43, 455401 (2010).

[81] H. Mizoguchi, H. W. Eng, and P. M. Woodward, Inorg. Chem. **43**, 1667 (2004).

[82] A. Prakash, et al. Nat. Commun. 8, 15167 (2017).

[83] Kim, H. J. et al. Phys. Rev. B 86, 165205 (2012).

[84] X. Luo et al. Appl. Phys. Lett. 100, 172112 (2012).

[85] H.J. Kim et al. Appl. Phys. Express 5, 061102 (2012).

[86] H. Paik et al. APL Mater. 5, 116107 (2017).

[87] K. Ganguly, A. Prakash, B. Jalan, C. Leighton, APL Mater. 5, 056102 (2017).

[88] E. McCalla, D. Phelan, M.J. Krogstad, B. Dabrowski, C. Leighton, Phys. Rev. Mater. 2, 084601 (2018).

[89] Z. Galazka et al. J. Phys. Condens. Mat. 29, 075701 (2016).

[90] S. Raghavan et al. APL Mater. 4, 016106 (2016).

[91] J. Shiogai, K. Nishihara, K. Sato, A. Tsukazaki, AIP Adv. 6, 065305 (2016).

[92] T. Stanislavchuk, A. Sirenko, A. Litvinchuk, X. Luo, S.-W. Cheong, J. Appl. Phys. 112, 044108 (2012).

[93] E. Moreira E. et al. J. Solid State Chem. 187, 186-194 (2012).

[94] W.-J. Lee et al. Annu. Rev. Mater. Res. 47, 391-423 (2017).

[95] S. James Allen, S. Raghavan, T. Schumann, K.-M. Law, S. Stemmer, Appl. Phys. Lett. 108, 252107 (2016).

[96] C.A. Niedermeier et al. Phys. Rev. B 95, 161202 (2017).

[97] H. Mizoguchi, H.W. Eng, P.M. Woodward, Inorg. Chem. 43, 1667-1680 (2004).

[98] S.A. Chambers, T.C. Kaspar, A. Prakash, G. Haugstad, B. Jalan, Appl. Phys. Lett. 108, 152104 (2016).

[99] X. Fan, W. Zheng, X.Chen, D.J. Singh, PLoS ONE 9, e91423 (2014).

[100] H. J. Kim, U. Kim, T. H. Kim, J. Kim, H. M. Kim, B. G. Jeon, W. J. Lee, H. S. Mun, K. T. Hong, J. Yu, K. Char, and K. H. Kim, Phys. Rev. B 86, 165205 (2012).

[101] H. R. Liu, J. H. Yang, H. J. Xiang, X. G. Gong, and S. H. Wei, Appl. Phys. Lett. 102, 112109 (2013).

[102] S. S. Shin, E. J. Yeom, W. S. Yang, S. Hur, M. G. Kim, J. Im, J. Seo, J. H. Noh, S. Seok, Science 356, 167-171 (2017)

[103] D. S. Ginley and C. Bright, MRS Bull. 25 (8), 15 (2000)

[104] A. Muthukumar, G. Rey, G. Giusti, V. Consonni, E. Appert, H. Roussel, A. Dakshnamoorthy, and D. Bellet, AIP Conference Proceedings 1512, 710 (2013)

[105] S. H. Lee, S. H. Han, H. S. Jung, H. Shin, J. Lee, J. H. Noh, S. Lee, I. S. Cho, J. K. Lee, J. Kim, and H. Shin, J. Phys. Chem. C 114, 7185–7189 (2010)

[106] K. K. Teshima, Y. Shirai, T. Miyasaka, J. Am. Chem. Soc. 131, 6050–6051, (2009)

[107] M. M. Lee, J. Teuscher, T. Miyasaka, T. N. Murakami, H. J. Snaith, Science 338, 643–647 (2012)

[108] J. Shin (2018) Mobility enhancement in wide band gap semiconductor $BaSnO_3$.

[109] P. G. Neudeck, R. S. Okojie, and L.-Y. Chen, Proceedings of the IEEE. 90, 1065 (2002).

[110] M. Islam, Solid State Ionics. 155, 75-85 (2002).

[111] W.S. Kim, E.O. Chi, J.C. Kim, N.H. Hur, K.W. Lee, Y.N. Choi, Phys. Rev. B 68, 172402 (2003).

[112] E.O. Chi, S. Kim, N.H. Hur, Solid State Commun. 120, 307 (2001).

[113] T. Tohei, H. Wadaa, T. Kanomatab, J. Magn. Magn. Mater 585, 272-276 (2004).

[114] P.M. Singer, T. Imai, T. He, M.A. Hayward, R.J. Cava, Phys. Rev. Lett. 87, 257601 (2001).

[115] E.O. Chi, S. Kim, N.H. Hur, Solid State Commun. 120, 307 (2001).

[116] C.M.I. Okoye, Mater. Sci. Eng. B 130, 101-107 (2006).

[117] M. Hassan, A. Shahid, Q. Mahmood, Solid State Communications, 270, 92-98 (2018).

[118] J. Nuss, C. M¨uhle, K. Hayama, V. Abdolazimi, and H. Takagi, Acta Cryst. B, 71(3), 300–312 (2015).

[119] A.Widera and H. Schäfer. Mater. Res. Bull., 15(12), 1805–1809 (1980).

[120] T. Kariyado and M. Ogata, J. Phys. Soc. Jpn., 80(8), 083704 (2011).

[121] T. Kariyado and M. Ogata, J. Phys. Soc. Jpn., 81(6), 064701 (2012).

[122] T. H. Hsieh, J. Liu, and L. Fu. Topological crystalline insulators and Dirac octets in antiperovskites.

[123] E. Atallah.E. Doctorate Thesis, Université Amar Telidji, Laghouat

[124] D. Cherrad, M. Maouche, M. Maamache, L. Krache Physica B 406, 2714-2722 (2011).

[125] T. Kariyado, M. Ogata, Phys. Rev. Mater. 1, 061201(R) (2017).

[126] P. J. W. Moll, N. L. Nair, T. Helm, A. C. Potter, I. Kimchi, A. Vishwanath and J. G. Analytis, Nature, 535, 266–270 (2016).

[127] T. Liang, Q. Gibson, M. N. Ali, M. Liu, R. J. Cava and N. P. Ong, Nat. Mater., 1, 280–284 (2015).

[128] T. Kariyado, M. Ogata, Physical Review Materials, 1(6), 061201 (2017).

[129] T. Kaur, M.M. Sinha, M. M. Materials Today Communications, 26, 101741 (2021).

[130] Y.F. Lee, F. Wu, R. Kumar, F. Hunte, J Schwartz, J. Narayan, Appl. Phys. Lett. 103, 112101 (2013).

[131] Y.J. Ma, A. Edgeton, H. Paik, B.D. Faeth, C.T. Parzyck, B. Pamuk, S.L. Shang, Z.K. Liu, K.M. Shen, D.G. Schlom, et al. Adv. Mater. 32, 2000809 (2020).

[132] M. Minohara, R. Yukawa, M. Kitamura, R. Kumai, Y. Murakami, H. Kumigashira, J. Cryst. Growth 500, 33–37 (2018).

[133] I. Hamberg, C.G. Granqvist, J. Appl. Phys. 60, R123 (1986).

[134] W. Lu, S. Jiang, D. Zhou, S. Gong, Sensors Actuators 80, 35 (2000).

[135] W.F. Zhang, J. Tang, J. Ye, Chem. Phys. Lett. 418, 174 (2006).

[136] B. Bellal, B. Hadjarab, A. Bouguelia, M. Trari, Theor. and Exp. Chem. 45, 172 (2009).

[137] N. Al-Dahoudi, H. Bisht, C. Gobbert, T. Krajewski, M.A. Aegerter, Thin Solid Films 392, 299 (2001).

[138] H. Mizoguchi, H.W. Eng, P.M. Woodward, Inorg. Chem. 43, 1667 (2004).

[139] K. Haddadi, A. Bouhemadou, L. Louail, S. Bin-Omran Solid State Communications 150, 1995-2000 (2010).

[140] D. Cherrad, D. Maouche, L. Louail, M. Maamache solid State Communications 150, 782-787 (2010).

[141] Y. Benkhetta et al Optik 127, 3005–3008 (2013).

[142] J.E. Hill and R.R. Chamberlin, US Patent 3, 148, 084 (1964).

[143] J. B. Mooney and S. B. Redding. Spray pyrolysis processing. – Annual Review Materials Science, 12, 81–101 (1982).

[144] D. Perednis, L.J. Gauckler, Journal of electroceramics, 14, 103-111 (2015).

[145] M. Maache, Doctorate Thesis, Universite Mohamed Khider-BISKRA, (2005).

[146] A. Hemier and W. Khamouli, Private communication (2019).

[147] H.H. Afify, S.A. Nasser, and S.E. Demian, J. Mater. Sci.: Materials in Electronics, **2**(3), 152 (1991).

[148] S. Mirzapour, S.M. Rozati, M.G. Takwale, B.R. Marathe, and V.G. Bhide, *J. Mater. Sci.*, **29**(3), 700 (1994).

[149] N.H.J. Stelzer and J. Schoonman, J. Materials Synthesis and Processing, **4**(6), 429 (1996).

[150] C.H. Chen, E.M. Kelder, and J. Schoonman, J. Eur. Ceram. Soc., **18**, 1439 (1998).

[151] H. Gourari, M. Lumbreras, R. Van Landschoot, and J. Schoonman, Sensors and Actuators B, **47**(1–3), 189 (1998).

[152] H. Gourari, M. Lumbreras, R. Van Landschoot, and J. Schoonman, Sensors and Actuators B, **58**(1–3), 365 (1999).

[153] M. Othemane, Doctorate Thesis (2018).

[154] J.L. Martínez, Doctorate Thesis, Université de Lille; Université de Mons (2020).

[155] B. Dennis, *Elements of X-ray Diffraction* (third ed. Prentice-Hall International, Upper Saddle River, N.J, London, 2000).

[156] W. Wei- Yu, J. N. Schulman, T. Y. Hsu, and F. Uzi, Appl, Phys. Lett, 50, 710,(1987).

[157] U. Platt, D. Perner, G. W. Harris, A. M. Winer, J. N. Pitts, Nature, 285, 312 (1980).

[158] C. Salim, Doctorate Thesis, Université Ferhat Abbas de Sétif 1 (2012).

[159] M.L. Kahina, Doctorate Thesis, Université Mouloud Maameri de Tizi Ouzou.

[160] J.I. Pankove, *Optical Processing in Semiconductors* (Courier Corporation, New York, 1971)

[161] N. Jafar, G. Murtaza, G. Nazir, A. Rehman, Journal of Materials and Physical Sciences, 2(2), 78-87 (2021).

[162] L. Belaidi, Doctorate Thesis, Université Frères Mentouri-Constantine 1).

[163] T. Baikie, Y. Fang, J.M. Kadro, M. K.Schreyer, F.Wei, S. G. Mhaisalkar, M. Graetzel and T. J. White, J. Mater.Chem. A 1, 5628-5641(2013).

[164] K. Abdelbaki, Doctorate Thesis, ENS Cachan France. (2014).

[165] C. Pollock, J. Lumin. 35, 65 (1986).

[166] M.J. Prajapati, R.V. Vardhan, S. Mandal, Ceram. Int. 45, 17420 (2019)

[167] T.P. Rao, M.C.S. Kumar, S.A. Angayarkanni, M. Ashok, J. Alloy Compd. 485, 413 (2009)

[168] A. Gholizadeh, J. Mater. Res. Technol. **8**, 457 (2019)

[169] R. Maa., S. Van Petegem, D. Grolimund, H. Van Swygenhoven, D. Kiener, G. Dehm, Appl. Phys. Lett. **92**, 071905 (2008)

[170] F. Bridier, J.-C. Stinville, N. Vanderesse, P. Villechaise, P. Bocher, Key Eng. Mater. 592–593, 493 (2014)

[171] A. Taschl, O. Kolednik, Mater. Sci. Eng. A342, 152 (2003)

[172] B. Budiansky, L. Truskinovsky, J. Mech. Phy. Sol. 41, 1445 (1993)

[173] G. Ahmed, A. Hashim, Silicon (2023). https:// doi. org/ 10. 1007/ s12633- 023- 02572-7

[174] W.O. Obaid, A. Hashim, Silicon 14, 11199–11207 (2022)

[175] R. Nasrin, H. Kabir, H. Akter, A.H. Bhuiyan, Results Phys. 9, 3357 (2020)

[176] M.T. Abdullah, L.M. Raoof, M.H. Abd, I.M. Mohammed, J. Phys. Conf. Ser. 1999, 012128 (2021)

[177] T. Zapletal, P. Sperka, I. Krupka, M. Hartl, Tribol. Int. 128, 356 (2018)

[178] C. Liu, Q. Guo, M. Wei, W. Ai, X. Xu, Opt. Express 28, 7772 (2022)

[179] K.H. Omran, M. Mostafa, M.S. Abd El-sadek, O.M. Hemeda, R. Ubic, Res. Phys. 19, 103850 (2020)

[180] O.B. Fadil, A. Hashim, Silicon 14, 9845–9852 (2022)

[181] A.F. Kadhim, A. Hashim, Opt. Quant. Electron. 55, 432 (2023)

[182] M. Minohara, R. Yukawa, M. Kitamura, R. Kumai, Y. Murakami, H. Kumigashira, J. Cryst. Growth 500, 33 (2018)

[183] R.S. Vemuri, M.H. Engelhard, C.V. Ramana, Appl. Mat. Interfaces 4, 1371 (2012)

[184] D.J. Wales, J. Grand, V.P. Ting, R.D. Burke, K.J. Edler, C.R. Bowen, S. Mintova, A.D. Burrows, Chem. Soc. Rev. 44, 4290 (2015)

[185] C. Fang, D. Wu, J. Xie, Y. Li, Y. Lou, Y. Pu, J. Mol. Struct. 1266, 133497 (2022)

[186] J. Batool, S.M. Alay-e-Abbas, G. Johansson, W. Zulfiqar, M.A. Danish, M. Bilal, J. Andreas Larsson, N. Amin, Phys. Chem. Chem. Phys. 23, 24878 (2021)

[187] X. Zhang, N. Han, C. Lin, Q. Wei, P. Zhao, Y. Cheng, W. Huang, Comp. Mater. Sci. 179, 109684 (2020)

[188] Y. Lei, L.D. Zhang, G.W. Meng, G.H. Li, X.Y. Zhang, C.H. Liang, W. Chen, S.X. Wang, Appl. Phys. Lett. 78(8), 1125 (2001)

[189] V.M. Longo, A.T. de Figueiredo, S. de Lazaro, M.F. Gurgel, M.G.S. Costa, C.O. Paiva-Santos, J.A. Varela, E. Longo, V.R. Mastelaro, F.S. De Vicente, A.C. Hernandes, R.W.A. Franco, J. Appl. Phys. 104(2), 023515 (2008)

[190] X.Y. Pan, M.Q. Yang, X.Z. Fu, N. Zhang, Y.J. Xu, Nanoscale 5, 3601